UNIVERSITY OF TWENTE.

Faculty of Engineering Technology,
Chair of Engineering Fluid Dynamics

Aerodynamic investigations of flatback airfoils and novel add-ons for modern wind turbine blades

Caterina Solombrino

Master Thesis
December 2023

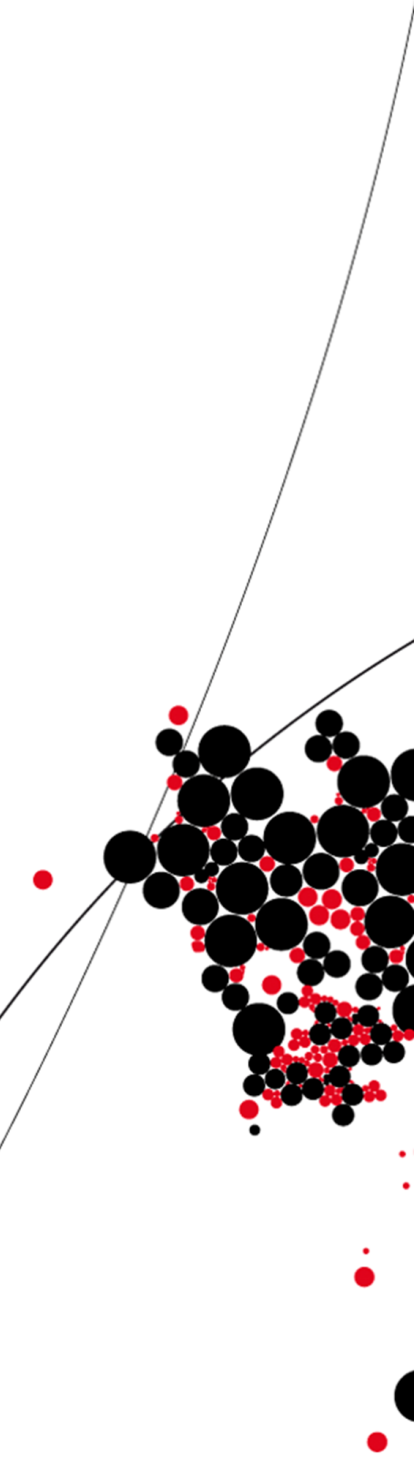

Document number:
EFD-439
Exam Committee:
prof. dr. ir. C.H. Venner (chair)
dr. H. Ozdemir (internal member)
dr. T. Weinhart (external member)
dr. A. Koodly Ravishankara (supervisor TNO)

Faculty of Engineering Technology,
Chair of Engineering Fluid Dynamics
University of Twente
P.O. Box 217
7500 AE Enschede
The Netherlands

Abstract

Modern wind turbines use longer blades to improve the annual energy production (AEP). Longer blades require thicker airfoils for structural integrity. Thicker airfoils are susceptible to issues like erosion, abrupt stalls, and early boundary layer transition, leading to increased drag and decreased lift, thus affecting overall performance.
Flatback (FB) airfoils offer structural and aerodynamic advantages, being stiffer, less sensitive to surface roughness and having a higher lift coefficient. Stiffer sections require less support, reducing weight and cost of the turbine blade. However, this comes with a drag penalty, mainly due to the increase in base drag. The low pressure near the wake causes vortex shedding, typical of bluff-body wake. The vibrations induced by the vortex shedding can not only increase the noise but also reduce the lifespan of the wind turbine.
Swallow tail add-on has been proposed to overcome these challenges by reducing the unsteadiness of the wake while maintaining the advantages of flatback airfoils. The objective of this research is to investigate the aerodynamics of flat back airfoils and add-ons such as swallow tail in a computationally efficient manner.

Acknowledgement

This master thesis represents the final part of my master program in Mechanical Engineering at the University of Twente (UT). The research, in the period from February 2023 to December 2023, has been carried out at TNO.

First, I would like to thank Akshay Koodly Ravishankara, my supervisor from TNO, for his availability, guidance and support. I would also like to thank my supervisor from UT, Huseyin Ozdemir, for offering me this opportunity and for his tutelage. I also really appreciate the freedom he gave to me to shape the project according to my interests. A special thanks also goes to the Professor Arne van Garrel for his knowledge and dedicating me time and support. Furthermore, I am sincerely grateful to my Professors Rob Hagmeijer, Edwin van Der Weide, Marten Toxopeus and Kees Venner for the very valuable learning experiences that brought me here. Their lectures not only have broaden my knowledge but also my passions and interests.

I would also like to thank my family and my boyfriend for their enormous support, patience and trust. In particular, I want to express my gratitude to my parents and brother, to which this work is dedicated. Finally, I would like to thank the people that made this journey at UT the most beautiful time of my life, people that from classmates became my Dutch family. Thank you Lorenzo, Umberto, René, Caky, Bert, Luke, Naman, Itzel. Thank you for the times spent in the cold corner of Waaier, for the study sessions at the library till closing, for the handing in of the assignments at 23:59 and for all the fun time together in Enschede.

Nomenclature

α	Angle of attack
AoA	Angle of attack
C_d	Drag coefficient
C_l	Lift coefficient
C_p	Pressure coefficient
U_∞	Free stream velocity
BEM	Blade element momentum theory
BET	Blade element theory
c	airfoil chord
DDES	Delayed detached eddy simulation
DES	Detached eddy simulation
EDDES	Enhanced delayed detached eddy simulation
FB	Flatback
HAWT	Horizontal axis wind turbine
LE	Leading edge
LES	Large eddy simulation
RANS	Reynolds averaged Navier Stokes
Re	Reynolds number based on chord length and free stream velocity
ST	Swallow tail
St	Strouhal number, based on trailing edge height
SW	Spanwise
TE	Trailing edge
URANS	Unsteady Reynolds averaged Navier Stokes

Contents

List of Figures

List of Tables

1 Introduction

In order to increase the annual energy production (AEP), modern wind turbine designs attempt to increase the blade length. Longer rotor blades sweep a larger area, capture more wind and hence, generate more power. However, this also increases the overall blade and rotor weight and hence, the experienced gravitational and aerodynamic loads.
Structural strength and stiffness could be gained by adopting thick airfoils in the inboard region of the blade. On the other hand, thick airfoils with sharp trailing edge present premature loss of laminar flow due to surface contamination. As a result, the achievable maximum lift is reduced [3].
With the aim of improving the poor aerodynamic performance of thick airfoils, the flatback airfoil (FB) concept has been introduced. Flatback airfoils results from blunting the trailing edge of thick airfoils. This concept, while keeping the structural benefits, has shown to have very interesting aerodynamic performances. By reducing the curvature near the trailing edge, the adverse pressure gradient is reduced and hence the premature flow separation alleviated. They indeed show less sensitivity to surface roughness and a higher maximum lift coefficient ($C_{L_{max}}$) and lift curve slope [6]. However, this comes with a drag penalty, mainly due to the increase in base drag. The low pressure near the trailing edge causes vortex shedding, typical of bluff-body wake, which result in high drag values. This drag penalty can be reduced by means of trailing edge add-ons which aim to increase this base pressure. In the literature, several trailing edge devices have been investigated and proven to improve the performance of flatback airfoils [7] [8] [9]. An innovative add-on, called "swallow tail", has also been proposed [10] [11]. This has shown to reduce the unsteadiness of the wake and thus, the drag.

The flow past a FB airfoil consists of a three-dimensional unsteady wake characterized with vortex shedding. A desirable tool for the research and design of flatback airfoils is computational fluid dynamic (CFD). However, this is very challenging given the complexity of the flow around a flatback airfoil and the limited availability of experimental data for validating the numerical results. For industrial applications, the Reynolds Averaged Navier-Stokes (RANS) and unsteady RANS (URANS) are the most widely used approaches, given the lower computational time compared to higher fidelity level methods. However, in case of highly unsteady and massively separated flow such as the flow around FB, RANS is not suitable [12]. On the other hand, higher fidelity approaches such as Large Eddy simulations (LES), requires a grid resolution that is prohibitive at practical Reynolds numbers (Re). Hence, as a compromise, hybrid RANS/LES approaches such as Detached Eddy Simulation (DES) are used, in which RANS is applied in the near wall region, and LES elsewhere. Furthermore, accurate predictions of the flow characteristics do not only rely on the fidelity level of the numerical approach but also on the mesh resolution and size of computational domain [13] [14].

The objective of the present study is to investigate the aerodynamics of flatback and swallow tail airfoils by means of efficient numerical simulations and assess their effect on the performance of wind turbine blades. In particular, a swallow tail design that develops from the patent application [10] will be proposed and the capability of this concept to overcome the drawbacks of the flatback investigated. Additionally, it is aimed to understand which fidelity level, mesh

resolution and computational domain are needed to accurately capture the flow phenomena involved. In particular 2D URANS, 3D URANS and 3D EDDES (Enhanced Delayed DES) as hybrid RANS/LES are the fidelity levels evaluated in this investigation.

In Chapter 2, a literature review covering the aerodynamics of wind turbines and flatback airfoils is given. The desirable airfoil characteristics for wind turbine applications are presented and the aerodynamic properties of the FB airfoil correlated to them. Furthermore, the numerical approaches suggested in the literature suitable to capture these properties will also be presented preceded by a numerical background of turbulent flows. After that, in Chapter 3 the objectives will be redefined and the research questions formulated. In Chapter 4, the methodology followed to answer the research question is outlined. Finally, the results, conclusions and recommendations of this study will be presented in Chapter 5, 6 and 7.
An schematic view of the airfoils involved in this study is given in Figure 1.1.

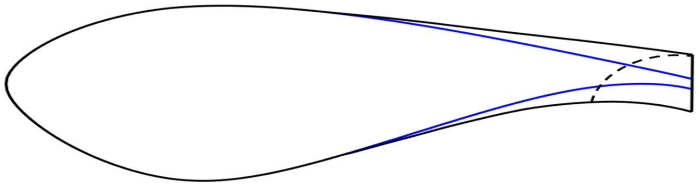

Figure 1.1: Schematic geometries of the involved airfoils: regular (blue), flatback (black), swallow tail (dashed)

2 Literature Review

In the development of wind turbines, aerodynamics and, particularly, airfoil design, plays an important role. This chapter provides an introduction to wind turbine aerodynamics, highlighting the relation between airfoil performance and wind turbine rotor performance. In particular, the characteristics to be considered when designing airfoils for wind turbine applications are described. Subsequently, how the aerodynamic properties of flatback airfoils meet these requirements is presented. Finally, the numerical approaches suggested in the literature suitable to capture the flow phenomena around flatback airfoils are reported.

2.1 Wind Turbine Aerodynamics

2.1.1 Airfoils and General Concepts

The cross sections of the rotor blades are airfoil shaped. Before introducing the correlation between airfoil and wind turbine performance, some general aerodynamic airfoil concepts are here described. The airfoil and its terminology are displayed in Figure 2.1a.

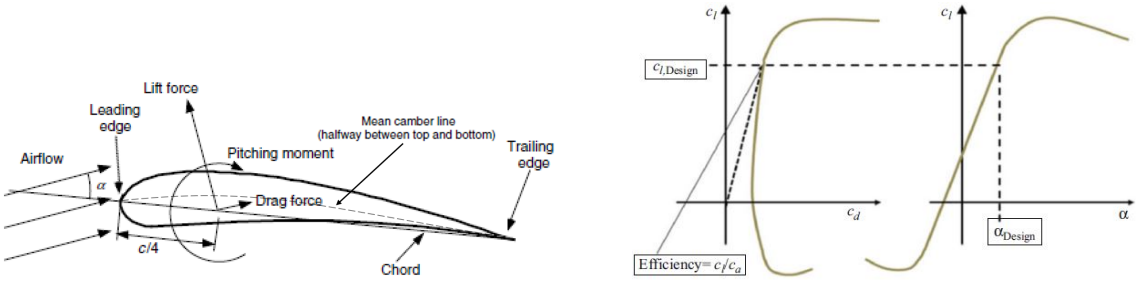

(a) Airfoil terminology, adapted from [1]

(b) Example of polars [15]

Figure 2.1: General airfoil concepts

The most forward point is called leading edge (LE) while the most rearward one is called trailing edge (TE). The chord (c) is the straight line connecting the two. The thickness (t) is the distance between the lower and the upper surface measured perpendicular to the chord. These surfaces are also referred as pressure and suction side respectively. The mean camber line represents the midway points, measured perpendicular to the mean camber line itself. The distance between the mean camber line and the chord, measured perpendicular to the chord, defines the camber. The span (l) is the length perpendicular to the airfoil cross-section (not visible in this 2D representation). The angle between the incoming airfoil and the chord line is the angle of attack α, also denominated as AoA. When the air flows over the airfoil surface it produces a distribution of forces. In particular, The pressure variation over the airfoil and the friction between the air and the airfoil generates the lift force (L) in the direction perpendicular to the relative velocity, the drag force (D) in the direction parallel to it and a pitching moment (M) that act at the quarter of the chord. These forces are usually expressed in the form of

non-dimensional coefficient as follow:

$$C_l = \frac{L/l}{\frac{1}{2}\rho U_\infty^2 c} \tag{2.1}$$

$$C_d = \frac{D/l}{\frac{1}{2}\rho U_\infty^2 c} \tag{2.2}$$

$$C_m = \frac{M}{\frac{1}{2}\rho U_\infty^2 A c} \tag{2.3}$$

where ρ is the air density, U_∞ the free stream velocity and $A = c \times l$ is the projected airfoil area. Another important non-dimensional coefficient is the pressure coefficient, defined as:

$$C_p = \frac{P - P_\infty}{\frac{1}{2}\rho U_\infty^2} \tag{2.4}$$

where P_∞ is the free stream static pressure and P the static pressure at the point where C_p is evaluated. Finally, the most important dimensionless parameter used to describe the flow conditions is the Reynolds number Re which is the defined as:

$$Re = \frac{\rho U_\infty L}{\mu} \tag{2.5}$$

where L is the characteristic length, in this case the chord, ρ and μ the density and dynamic viscosity of the fluid, in this case air.

Polar plots are used to summarize the characteristics of airfoils. These plots show change in lift and drag coefficient with angle of attack and lift versus drag coefficient. An example is given in 2.1b, where the dashed line in the left plot is a measure of the airfoil efficiency (C_l/C_d): the steeper the line, the more efficient is the airfoil. The tangent point determines the design lift coefficient $C_{l,Design}$ corresponding to the design angle of attack α_{Design}.

2.1.2 Wind turbine and airfoil performance

Wind turbines are machines designed to convert the kinetic energy of the wind to mechanical power. The extraction of the kinetic energy from the wind is done by the rotor blades and can be done in different ways: rotor driven by the lift on the airfoils and rotor driven by the drag on the blades. Hence, the power production is strictly related to the rotor performances and, in particular, to the aerodynamic efficiency of the blades. This research focuses on lift driven horizontal axis wind turbine (HAWT), being this the most common concept used today[16].
The Blade Element Momentum Theory (BEM) is here considered to describe the main characteristics of the airflow around wind turbine blades and outline the relation between airfoils and the power production.

To predict rotor performance, the BEM combines the 1-D momentum theory and the blade element theory. Using the 1-D momentum theory and the actuator disc model, the wind turbine rotor is modelled as an actuator disc with an infinite number of blades (Figure 2.2a) in which the disc exerts a thrust force T on the wind flow and hence reducing its speed. The extraction of kinetic energy from the wind is achieved with this reduction in flow speed from the free stream velocity U_∞ to $U_\infty(1-a)$ in the rotor plane, where a is the axial induction factor representing the fractional decrease in axial wind speed from free stream to rotor plane. Introducing the Blade Element Theory (BET), the rotation of the disk can be included in the analysis. In the BET, the blade is assumed to be divided in sections (Figure 2.2b), airfoil shaped, where the thrust and the torque are expressed in terms of lift and drag coefficient (C_l, C_d) and the angle

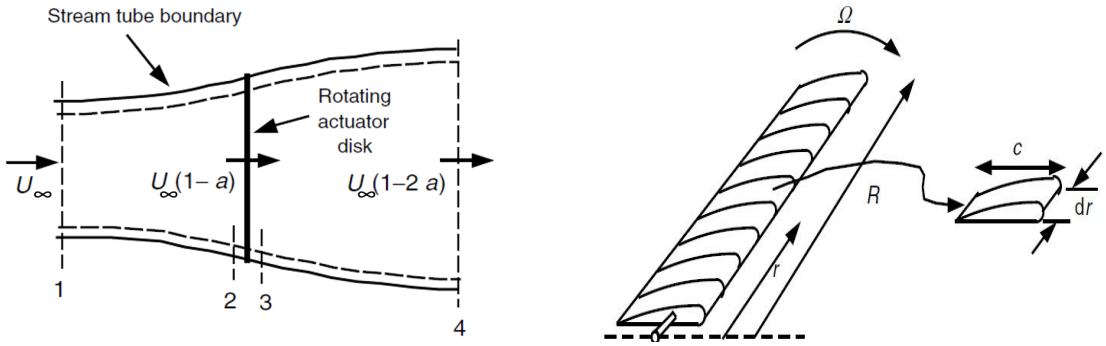

(a) Actuator disc model (b) Schematic of blade elements

Figure 2.2: Rotor analysis by means of BEM theory, adapted from [1]

of attack (AoA). Considering the element at radius r, the relative wind speed W is given by the sum of the velocity at the rotor, $U_\infty(1-a)$, and the wind velocity due to blade rotation. This rotational component is derived using the conservation of angular momentum. As reaction to the torque imparted by the flow on the rotor, the rotor exerts a torque on the flow behind it inducing wake rotation. Hence, the tangential velocity of the air relative to the blade increases from Ωr to $\Omega r(1+a')$, where Ω is the angular velocity of the rotor and a' the tangential induction factor representing the increase in tangential velocity of the air relative to the blade due to wake rotation.
This analysis shows that the blade section experiences a relative wind speed W, given by the sum of the axial and tangential velocity, with an inflow angle to the rotor plane Φ and an angle of attack α to the chord line c. The angle from the rotor plane to the chord line is the twist angle θ. The velocity triangle and resulting forces for an sectional element of a rotating wind turbine blade are displayed in Figure 2.3.

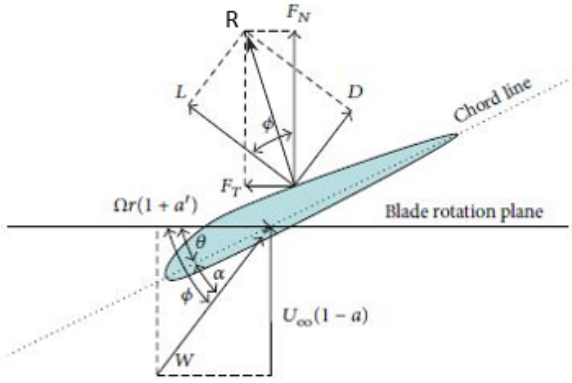

Figure 2.3: Velocity and forces triangles for a rotating wind turbine blade section [2]

As the air flows over the blade section at relative speed W and with an inflow angle Φ, lift and drag forces are generated of which the resultant vector R, represents the total aerodynamic force. The component of this force normal to the rotor plane (F_N) is the one contributing to the thrust while the component tangential to the rotor plane (F_T) is the one contributing to the torque. The thrust is the force responsible of blades bending, thereby source of structural concerns. The torque is the force governing the blades rotation and hence the power generation. Expressions of these forces, as function of C_l and C_d, are obtained by first projecting the lift and drag in the directions normal and tangential to the rotor plane:

$$F_N = Lcos\phi + Dsin\phi \tag{2.6}$$

$$F_T = Lsin\phi - Dcos\phi \tag{2.7}$$

Subsequently, equations 2.6 and 2.7 are made non-dimensional dividing by $\frac{1}{2}\rho W^2 c$, yielding to the force coefficients of the annular elements:

$$C_n = C_l cos\phi + C_d sin\phi = C_l\Big(cos\phi + \frac{sin\phi}{C_l/C_d}\Big) \tag{2.8}$$

$$C_t = C_l sin\phi - C_d cos\phi = C_l\Big(sin\phi - \frac{cos\phi}{C_l/C_d}\Big) \tag{2.9}$$

From these expressions it is clear that normal and tangential force coefficients C_n and C_t, and hence the rotor performances, are directly correlated to the airfoil design. In particular, Equation 2.9 highlights how wind turbine blades use airfoils to generate power: the larger the ratio C_l/C_d the larger C_t. Furthermore, the closer the airfoil section is to the tip, the more important is C_l/C_d. This can be seen by looking at Figure 2.3 and using trigonometry correlations to express the inflow angle as given in Equation 2.10.

$$\phi = arctan\left(\frac{U_\infty(1-a)}{\Omega r(1+a')}\right) = arctan\left(\frac{(1-a)}{\frac{\lambda r}{R}(1+a')}\right) \tag{2.10}$$

Where λ is the tip speed ratio defined as $\lambda = \frac{\Omega R}{U_\infty}$. From Equation 2.10, it is clear that the larger $\frac{\lambda r}{R}$ (the closer to the tip), the smaller is ϕ and the more the performance are influenced by C_l/C_d.

This analysis described the aerodynamic efficiency of an annular element of a wind turbine blade. However, there are more aspects to be considered in the airfoil design and that affect wind turbine performances such as loads, structural stiffness and noise emission. Below, the 2D airfoil characteristics (C) needed for achieving high wind turbine performance, including aerodynamic efficiency are given.

(C.1) High aerodynamic efficiency: high C_l/C_d, especially on the outer part of the blade.

(C.2) Low leading edge (LE) roughness sensitivity: small variation in maximum lift coefficient $C_{l,max}$ whether the airfoil is under free or forced transition. When the blade leading edge gets roughened by damage and debris the power output can drop as much as 40% due to decrease in $C_{l,max}$ and increase in C_d [1].

(C.3) Small $C_{l,min}$, especially on the outer part of the blade: at high wind speed for a pitch-regulated wind turbine or in case of shutdown the load and deflection towards the tip depends on $C_{l,min}$.

(C.4) Choice of $C_{l,max}$: if a high $C_{l,max}$ is chosen, a smaller chord is needed and vice-versa. A small chord is an advantage for the projected blade area and hence for the standstill loads. However, it is a disadvantage for the structure.

(C.5) Smooth stall behaviour: it is important to obtain as high forces in post stall as possible because they will be smaller than $C_{l,max}$. During stall the turbulent and separated flow induces fluctuating flow conditions and hence loads on the wind turbine.

(C.6) Shedding frequency: the non-dimensional Strouhal number St is used to characterize the vortex shedding noise frequency f_s. This is defined as $St = f_s L/U_\infty$, where L is the characteristic length. When the shedding frequency is close to a natural frequency of the blade, vortex shedding vibrations will occur, with repercussions on the noise emissions and structural damage.

(C.7) Structural strength and stiffness: larger sectional area and moment of inertia
The structure needs to withstand the high aerodynamic and gravitational loads, especially with increasing rotor size: the larger C_l/C_d the larger the torque but also the thrust loads. In particular, the generated thrust is higher than the torque (Equation 2.8).

Finally, to be accepted in the marketplace, the development of any wind turbine component, including airfoil design, should not only increase the energy production but also reduce the costs.

2.2 Aerodynamics of Flatback airfoils

From section 2.1.2 it is clear that wind turbine must be designed to convert as much wind kinetic energy into torque as possible while ensuring structural strength and stiffness and in a cost-effective manner. As wind turbines increase in size, structural concerns become important: blade mass increases with approximately the cube of the blade length [3]. Hence, larger wind turbines not only induce larger aerodynamic loads, but also larger mass and gravitational loading. For this reason, thick airfoils (i.e., airfoils with thickness to chord ratio $t/c \geq 0.25$) have been adopted in the inboard sections of the blades. They allow to envelop deeper spars and hence enhance structural integrity (C.7). However, thick airfoils with sharp trailing edge (TE) (i.e. trailing edge thickness $t_{TE}/c < 0.05$) have poor aerodynamic performances in particular in terms of C_l/C_d (C.1) and sensitivity to surface contamination (C.2): the premature loss of laminar flow under soiled conditions results in an decrease in maximum lift (C.4) [3]. Although the inboard region of the blade may not play a major role in generating torque, any improvement in aerodynamic efficiency contributes to the overall power output of the wind turbine.
Hence, designers have proposed thick airfoils with blunt trailing edge, also referred as thick trailing edge or flatback airfoils (FB). Blunting the trailing edge reduces the curvature near the trailing edge and allows for a substantial portion of the pressure recovery to take place in the wake. This results in a reduction of the adverse pressure gradient on the suction surface and, consequently reduces the sensitivity to premature separation and increases the $C_{L,max}$. This is primarily important in the inboard region of the blades where the thick boundary layer linked to the low Re is susceptible to flow separation. However, this comes with a drag penalty mainly due to the increase in base drag: the low pressure behind the trailing edge causes vortex shedding, typical of bluff-body wake [17]. Furthermore, this unstable and unsteady wake might result in abrupt stall [6] [18].

Already in the 80s, wind tunnel experiments of a $NACA\ 64-621$ airfoil with trailing edge truncated (TET) showed the potential of this concept [19]. Compared to other thick airfoils with sharp trailing edge, the $NACA\ 64-621\ TET$, showed a higher $C_{l,max}$, a higher lift curve slope and lower surface roughness sensitivity. However, the maximum lift-to-drag ratios resulted to be better for the airfoils with sharp TE. Indeed, due to the blunt TE, the drag values at low angles of attack are much higher than the values for sharp TE. This is due to the base drag: at low angles of attack, base drag resulted to be 60% of the measured pressure drag, while its influence on total pressure drag decreased with increasing angle of attack.

A more recent study [3], demonstrates the optimal way to generate a blunt trailing edge airfoil and the potential advantages of FB. Generally, FB are created by cutting off a specific amount of the rear portion of a baseline airfoil and then rescaled to unit chord length. However, this results in an increase in t/c and camber loss, thus negatively affecting the lift characteristics. To isolate the favorable effect of blunting the trailing edge, the original airfoil should be modified by symmetrically adding thickness to both side of the camber line as shown in Figure 2.4. In this way, the maximum thickness and camber are unvaried. The numerical results of this study showed the benefits of this method: increased $C_{l,max}$ and lift curve slope and decreased

sensitivity to premature boundary layer transition.

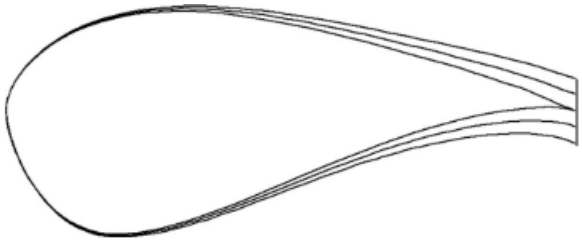

Figure 2.4: Optimal way to generate flatback airfoil from regular one[3]

These findings were confirmed experimentally in another investigation where also the trailing edge thickness (t_{TE}) was noted to exert an influence on the airfoil's performance [6]. It is recommended to limit the ratio $(t-t_{TE})/c$ to approximately 20%. In this way, the reduction of the adverse pressure gradient on the suction surface is ensured and hence, the achievable lift performance under soiled conditions. Three TE thicknesses ranging from 0.5% to 17.5% chord were tested. The experimental results showed that the sharp TE airfoil with TE thickness of $0.5\%c$ had the highest C_l/C_d under free transitions but, under tripped conditions, the lift characteristic degraded. On the other hand, the larger the TE thickness, the more the leading edge roughness sensitivity is reduced and hence, the larger the $C_{l,max}$. However, this comes with an increase drag, mainly due to base drag, and an abrupt stall. As a result, under fixed transition, the airfoil with TE thickness $17.5\%c$ exhibited the lowest efficiency while the one with TE thickness $t = 8.75\%c$ achieved the best performances.

To address the drag penalty, an experimental investigation of six different TE devices for the airfoil with $17.5\%c$ TE thickness has been carried out [8]. These TE modifications, "splitter plate", consisted of L-shaped metal plates mounted perpendicularly to the T. Two configurations, one involving a single plate and one consisting of two plates, with different edge treatments were tested. Drag reductions of 50% for low angle of attack and up to 25% were achieved with the single and double splitter plates respectively. Edge treatment affected only the double splitter configuration. These edge treatments also affected the lift characteristics. The single splitter plate experienced a lower maximum lift. On the other hand, the double splitter plate showed an increase in lift curve slope, probably due to the chord increase, and an increase in zero lift angle, likely due to the decrease in camber. It is then suggested to align the double splitter plates with the camber line of the airfoil.
Another study on drag-reduction devices [9] confirms how these TE treatments improve the performances of FB airfoils. Additionally, this investigation provides valuable insights into the flow mechanisms responsible for achieving this drag reduction and which parameters are involved. The low pressure near the wake causes vortex shedding, typical of bluff-body wake, resulting in this base drag increase. Hence, TE devices aim to increase the base pressure. The splitting plate aims to "split" the two alternating vortices originating from the TE or delay this merging. The vortex formation length is extended away from the base surface in such a way that the large flow variations caused by the vortex shedding are transformed into smaller and quicker variations. This means that the shedding occurs at higher frequency and with smaller amplitude. This is reflected in an increase of the Strouhal (St) number. Typically, the vortex shedding at the TE of FB airfoils occurs at $St \approx 0.24$. Amongst the TE drag-reduction devices tested in this study, the highest measured Strouhal number was $St = 0.35$. While it is proved that these frequency and amplitude shifts reduce the base drag, the effect on noise and structural damage still needed to be investigated.
Finally, an innovative concept to reduce the drag of FB airfoils, "swallow tail" (ST), has been developed [10]. The working principle is different from the splitting plates previously mentioned.

The ST has two sharp extensions with different lengths that suppress the coupling between the vortex from the upper and lower surface. Indeed, when the flow separates from the shorter side it merges more smoothly with the flow on the upper side. As a result, the wake unsteadiness is reduced and hence the base drag and noise. This concept has proven both numerically and experimentally to reduce drag up to 40% [18] [11]. No significant change in lift performances was observed. However, this might be due to the fact that the swallow tail has been attached as an extension to the blade, meaning that there is an increase in chord length and a change in camber.

Lastly, an extensive experimental analysis from the Sandia National Laboratories presents the aerodynamic and aeroacoustic properties of a flatback version of the TU Delft DU97-W-300 [7] [20]. The DU97-W-300-FB was generated by adding thickness to the aft half of the airfoils, resulting in a blunt TE thickness of $10\%c$.
When compared to the standard DU97-W-300, the results showed an increase in lift-curve slope and $C_{l,max}$ at both low and high Reynolds number as well as a reduced sensitivity to LE soiling. The increase in drag was reduced up to 50% with a splitter plate attachment.
This is reflected in the pressure distributions. At low AoA of the DU97-W-300-FB pressure distribution overlap with the one of the DU97-W-300 till it plateaus near the TE: while the standard airfoil pressure recovers to free-stream pressure, the FB ends at a lower pressure. At high AoA, the FB suction surface is overall lower than the one of the standard airfoil. As previously mentioned, this low pressure is the cause of the base drag. When a splitter plate is included in the FB, the magnitude of the suction peak slightly grows and, at low AoA, the suction surface pressure at the TE increases.
With regard to the aeroacoustic characteristics, due to the vortex shedding, the FB airfoil presents higher noise. Indeed, the aeroacoustic measurements confirm the presence of a vortex shedding tone at $St \approx 0.24$, which shifts to $St \approx 0.30$ when a splitter plate is attached.
In conclusion, flatback airfoils have proven to meet both aerodynamics and structural requirements, namely (C.2),(C.4),(C.7). This means that flatback airfoils have the potential to be cost-effective: the larger sectional strength allows to reduce weight and hence costs while the aerodynamic performances can increase the energy production.
Furthermore, with the integration of TE devices, it is possible to overcome the drawbacks of this concept and hence also retain the advantages of a sharp TE airfoil (C.1), (C.6). This implies that flatback airfoils could also be adopted in the outboard region of the wind turbine.

2.3 Numerical Background

2.3.1 Turbulent flow

Wind energy industry relies on BEM-based methods for the design of wind turbine blades [15]. The inputs of these methods are the lift and drag polars of each sectional element of the blade, meaning that an accurate prediction of the airfoil aerodynamic characteristics at all the sectional operational conditions plays an important role. These characteristics can be derived using Computational Fluid Dynamics (CFD) simulations.
Wind turbines mainly operate in turbulent flow and at a diverse range of local Reynolds numbers (up to $Re = 10^7$ at the tip). Turbulent flows are highly unsteady, three dimensional and fluctuate on a wide range of length and time scale. For this reason, numerical simulation of turbulent flows is very challenging .

There are mainly three approaches to model turbulent flows [4]:

1. RANS: the Reynolds Averaged Navier Stokes is the most widely used method where time averaged Navier-Stokes equations are solved and the effect of turbulence is modelled on mean flow properties. The resulting equations are then steady. If the averaging is done

over ensembles, a set of statistically identical realizations, then the approach is called unsteady RANS (URANS) and the resulting equations may be unsteady. In Figure 2.5 the difference between these averaging methods is displayed, where it is clear that, if the flow is unsteady, time averaging (RANS) cannot be used. In any case, no turbulence is resolved, making any Reynolds-averaged model the cheapest in computational time and the lowest in fidelity level.

2. DNS: the Direct Numerical Simulation method fully solves the Navier-Stokes equations for all the turbulent length and time scales. For this reason, it is the most accurate approach but also very expensive in terms of computing resources and hence not practical for industrial applications.

3. LES: the Large Eddy Simulation approach, a compromise between RANS and DNS, solves the large scale motions of the flow while modelling the small scale ones using a subgrid-scale(SGS) model. However, the required refined grid resolution makes this method not applicable at practical Reynolds number.

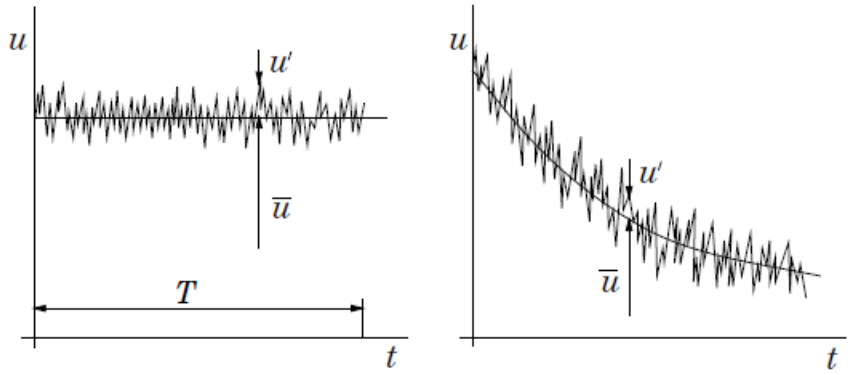

Figure 2.5: Reynolds averaging: time average of a statistically steady flow (left) and ensemble average of an unsteady flow (right) [4]

RANS Turbulence Models

In the Reynolds averaging approach, any flow property ϕ is described as the sum of a mean $\bar{\phi}$ and a fluctuating part ϕ':

$$\phi(t) = \bar{\phi} + \phi'(t) \tag{2.11}$$

Similarly, the decomposition of the velocity vector u (see also Figure 2.5) and the pressure P can be written as follow:

$$u(t) = \bar{u} + u'(t) \tag{2.12}$$

$$P(t) = \bar{P} + P'(t) \tag{2.13}$$

Substitution of these expressions in the Navier-Stokes equations yields to additional terms, forming the so called Reynolds-Averaged Navier Stokes equations. In particular, the substitution of Equation 2.12 in the momentum equation gives rise to an additional stress terms "Reynolds Stresses". The presence of these additional unknowns means that the system of equations is not closed. The closure of the system of mean flow equations requires the use of approximations: turbulence models.

Many turbulence models are based on the Boussinesq hypothesis for which the effect of turbulence can be represented as an increased viscosity. The total viscosity μ_{tot} is divided into a laminar μ_{dyn} and a turbulent component μ_{turb} :

$$\mu_{tot} = \mu_{dyn} + \mu_{turb} \tag{2.14}$$

The laminar viscosity is assumed to satisfy Sutherland's law while the turbulent viscosity is computed using a turbulence model [21]. The most common turbulence models are the one equation Spalart-Almaras (SA) model [22] and the two equation $k - \omega$ SST model [23]. The number of equations indicates the number of additional equations being solved. The SA model, solves a single conservation equation for the turbulent viscosity. It is suitable for flows with mild separation. The SST model consists of two equations: one for the turbulent kinetic energy and one for the turbulence scale. This model has proven to have satisfactory performance for modelling fully turbulent flows around airfoils [24].

Hybrid RANS/LES

Another commonly used approach is the Detached Eddy Simulation (DES) [25], hybrid RANS-LES turbulence model developed for the prediction of massively separated flow. This model applies RANS and the LES depending on the local RANS and LES turbulent length scales: in the near wall region, being the flow basically laminar, the RANS formulation is applied while on separated regions, the LES treatment is used. This means that a finer mesh is needed for correctly resolving the LES part.
The DES formulation is based on the SA turbulence model for computing the near wall distance d. The SA model originally contains a destruction term for its eddy viscosity $\tilde{\nu}$, proportional to $(\tilde{\nu}/d)^2$. In the DES formulation, the wall distance d is replaced by a modified wall distance term $\tilde{d}$ defined as:

$$\tilde{d} = min(d, C_{DES}\Delta) \tag{2.15}$$

$$\Delta = max(\Delta_x, \Delta_y, \Delta_z) \tag{2.16}$$

In Equation 2.15, C_{DES} is a model constant and Δ, the subgrid length scale, is defined in Equation 2.16 as the local largest grid spacing in all three directions . In the near wall region where $d < C_{DES}\Delta$ the flow is modelled by RANS while it is resolved by LES elsewhere.
This approach works when the grid spacing parallel to the wall $\Delta_{||}$ is larger than the boundary layer thickness δ. However, when $\Delta_{||} < \delta$ because of grid refinement or thickening of the boundary layer, DES can exhibit an incorrect behaviour: the LES mode is erroneously activated inside the attached boundary layer region where the resolution is not fine enough to fully support it. This generates inappropriate turbulent content in the regions where the flow was supposed to be resolved, leading to reduced turbulent stresses ("Modelled Stress Depletion", MSD). The depleted stresses reduce the skin friction, potentially resulting in premature separation ("Grid Induced Separation", GIS).
For this reason, Delayed DES (DDES), a new version of the DES technique has been proposed [26]. This formulation is able to detect the boundary layer hence ensuring the RANS behaviour in this zone and *delaying* the activation of LES mode even on ambiguous grid densities. This can be accomplished by modifying the definition of $\tilde{d}$ as follow:

$$\tilde{d} = d - f_d \; max(0, d - C_{DES}\Delta) \tag{2.17}$$

where f_d is a coefficient that is dependent on the local flow physics, local solution and wall distance, thus able to avoid undesirable switching to LES. In particular, $f_d = 0$ in RANS zones and $f_d = 1$ in all the other regions.
However, this formulation does not resolve the so called "grey area issue", denoting the inability of the DES or DDES approach to neither solve or model the turbulence in the RANS-LES

interface where $\Delta = d$. This causes a delay in the formation of instabilities, preventing an appropriate representation of turbulence in the initial regions of the free shear layers [27]. The origin of this issue is associated with the anisotropic grids typically used in DES (more refined in the streamwise direction and coarser in the spanwise) and can be mitigated with a different definition of the SGS length scale Δ [28]. This enhanced version of DDES, EDDES, proposes two subsgrid length scale definitions: $\tilde{\Delta}_\omega$ and Δ_{SLA}. A recent study [29] has investigated the influence of the SGS length scales on the flow physics and resolution, concluding that the Δ_{SLA} gives the best wake resolution in a massively separated wake.

2.3.2 Flow past a flatback airfoil

The flow past a FB airfoil consists of a three-dimensional unsteady wake characterized with vortex shedding. Therefore, numerical investigations of this flow is challenging, also given the limited availability of experimental data for validating the numerical results.
Accurate predictions of force coefficients and wake characteristics rely on the fidelity level of the numerical approach, mesh resolution, and the size of the computational domain.
The URANS approach is found to be dissipative and not suited to predict the unsteady and separated flow past flatback airfoils [12]. Previous 2D investigations of FB airfoils indicate that the linear region of the lift coefficient is generally well captured, while the prediction of $C_{l,max}$ and stall behaviour requires more sophisticated turbulence modelling [3] [6].
In another study [13], the flow past a 30% airfoil with a 10% thick TE is analyzed with 3D simulations employing both URANS and DDES and compared with wind tunnel data. The computational domain consists of identical grids of varying density with the spanwise direction extruded to one chord length. On the finer grids, there is a good agreement between the loads predicted by the URANS and DDES simulations. However, although the mean C_l and C_d values are similar between the two methods, the URANS results are qualitatively different from the DDES ones. The C_l time histories from the URANS simulations show unphysical load fluctuations as well as the flow visualisations reveal 2D-like vortical structures. This because URANS tends to underpredict turbulence levels and artificially restrict flow three-dimensionality, predicting 2D-like wake flows. On the contrary, in the DDES analysis the 3D character of the wake is captured even on the coarser grid, with more flow features resolved as the grid is refined. Finally, in a follow-up analysis [14], it has been shown that the spanwise length has to be at least $0.5c$ for the 3D phenomena involved in this flow to develop unrestrained. This is even more important at low AoA and beyond AoA of $C_{l,max}$ where the wake has been observed to be stronger and highly three-dimensional.

In conclusion, when the flow is mainly attached, URANS solutions can provide accurate load predictions. However, in case of highly unsteady and massively separated flow, URANS fails to capture flow phenomena that are important for the evaluation of stall and drag performance. If the wake details such as the turbulent fluctuations are of interest, higher fidelity level approaches (i.e. DDES) in combination with a 3D computational domain with sufficient spanwise length are needed. This is the case for the investigation of the flow past a flatback airfoil for wind turbine applications, where the analysis is not limited to an accurate prediction of the aerodynamics coefficients (see (C.1) - (C.7) Section 2.1.2).

3 Motivation and Goals

The literature review indicates that flatback airfoils have the potential to increase the energy production of wind turbines while reducing weight and hence, costs. Furthermore, the drag penalty and the higher noise can be overcome with the integration of TE devices, thereby improving the overall performance. In particular, swallow tail add-on has been proposed to overcome these challenges by reducing the unsteadiness of the wake while maintaining the advantages of flatback airfoils. If the potential of this concept is further proven, its adoption can be extended and hence the larger power demand addressed.

This research aims to investigate the aerodynamics of flatback airfoils and add-ons such as swallow tail in a computationally efficient manner and to answer the following research questions:

1. *Does the swallow tail concept overcome the drawbacks of flatback airfoils?*
2. *Which fidelity level and computational domain are needed to predict the aerodynamics of flatback and swallow tail airfoils?*

In order to do so, a computational set-up that is able to capture the aerodynamics of flatback airfoils while keeping the computational cost low needs to be researched. Hence, the appropriate fidelity level and mesh resolution needed to capture the complexity of this flow is first investigated. After that, it will be possible to assess the flow phenomena neglected by lower fidelity approaches and their importance in the prediction of the airfoil aerodynamic performance.
Once a suitable set-up (computational grid and numerical framework) is found, it will be used to evaluate the potential advantages of flatback airfoils and the capability of the swallow tail concept. Finally, a parameterization of the swallow tail geometry will be conducted to showcase the achievable performance.

Hence, the research questions can be worked out with the following objectives and derivables:

I. Research of a suitable computational grid

II. Research of a a suitable and efficient numerical framework

III. Design of swallow tail geometry with the appropriate set-up based on I. and II.

IV. Polars of the flatback and swallow tail geometries

4 Methodology

In this chapter the method used to conduct this research is presented. First, the geometries investigated in this study are given. Next, the computational methodologies such as flow solver and grid are introduced. Finally, the workflow followed to answer the research questions is displayed.

4.1 Geometries

The airfoils investigated in this study are the DU97-W-300 with sharp trailing edge [5] and its flat back version [7]. These will also be referred as "standard" or "regular" and "FB" or "blunt TE" respectively. The DU97-W-300 has a maximum thickness of 30%. The DU97-W-300-FB was generated by adding thickness to the aft half of the standard airfoil, resulting in a blunt TE thickness of $10\%c$. The reason why these airfoils have been chosen is because of the large availability of experimental data against which the numerical results can be compared and validated.
The geometry of the standard airfoil was available internally, while the FB version was obtained by digitizing the geometry from the literature [7]. To reduce the influence of this digitization on the comparison between standard and FB, only the aft-half of the FB airfoil was digitized. Subsequently, the merging with the standard front part has been smoothed in MATLAB (method "sgolay") [30].
Regarding the swallow tail concept, two geometries will be designed starting from the conceptual description given in the patent application [10]. These will also be referred as "ST1" and "ST2" or simply "ST".
Finally, the standard airfoil and the swallow tail conceptually have sharp edges. However, a finite edge ($\approx 0.017c$) has been employed for two reason:

1. The physical blade section has a finite TE thickness.
2. To avoid grid changes when comparing the performance of these airfoils numerically. An airfoil with sharp trailing edge requires a distinct grid topology (C-mesh) compared to an airfoil with finite/blunt trailing edge (O-mesh) [31] [6].

4.2 Flow solver SU2

The solver used to carry out the simulations is the open source software SU2 [32] [33] [21]. The governing equations are discretized following the method of lines, where the integration in space is carried out with the finite volume method while the time integration can be implemented with various methods. The resulting partial differential equation have the following structure [33]:

$$\partial_t U + \nabla \cdot F^C - \nabla \cdot F^V = Q \tag{4.1}$$

where U represents the vector of state variables, $F^C(U)$ and $F^V(U)$ are the convective and viscous fluxes and $Q(U)$ the source term. The boundary conditions (BC) will be detailed for each test case while the initial conditions are given in Table 4.1, which differ depending on the

Reynolds number.

In this study, the second order numerical scheme Jameson-Schmidt-Turkel (JST) has been used to discretize the convective fluxes. With regards to the viscous fluxes, the spatial gradients have been computed using Green-Gauss and weighted least-squares methods for the 2D and 3D simulations respectively [21]. For the source terms, a piecewise linear reconstruction is used.
Time integration is carried out with a second order dual time stepping approach [34] in combination with the implicit Euler scheme [21].
Finally, the turbulence closure equations are solved with a first order scalar upwind method with the application of both the SST and SA turbulence models.
The above mentioned numerical settings are applied throughout all the performed simulations unless differently specified. Where needed, more details will be given in the results chapter.

All the simulation cases are fully turbulent. The fidelity levels investigated in this study are:

- 2D RANS and 2D URANS for the standard airfoil and 2D URANS for the FB and swallow tail airfoils.
- 3D URANS and 3D EDDES as hybrid RANS/LES method for the FB and 3D EDDES for swallow tail geometry.

The results in terms of aerodynamic coefficients for the URANS and EDDES cases will be given as average values computed with an embedded windowed-time-averaging method ("Hann square").

Variable	**Unit**	**value**	**value**
Re	$-$	1.6×10^6	3×10^6
U_∞	m/s	23.536	44.130
ρ	kg/m^3	1.225	1.225
$Mach$	-	0.069	0.130
c	m	1	1

Table 4.1: Initial conditions

4.3 Computational Grids

For the mesh generation, the software Pointwise has been used [35]. All the airfoils are meshed with a structured O-mesh, for which an example is given in Figure 4.1.
Three grids with different number of nodes around the airfoil surface have been tested: 128, 258, 516. The initial cell height is set to achieve a $y+ \approx 1$ for an appropriate resolution of the viscous sublayer. The grow rate is 1.1 for the 2D URANS cases. For the EDDES simulations, a higher grid resolution is needed for the LES mode to appropriately resolve the flow. Hence, for the 3D cases a grow rate of 1.05 is used for the near airfoil region and 1.08 in the rest of the domain. In the spanwise direction, a constant spacing of 0.05 is used. Two spanwise sizes will be tested. More details will be given in the individual test case sections.

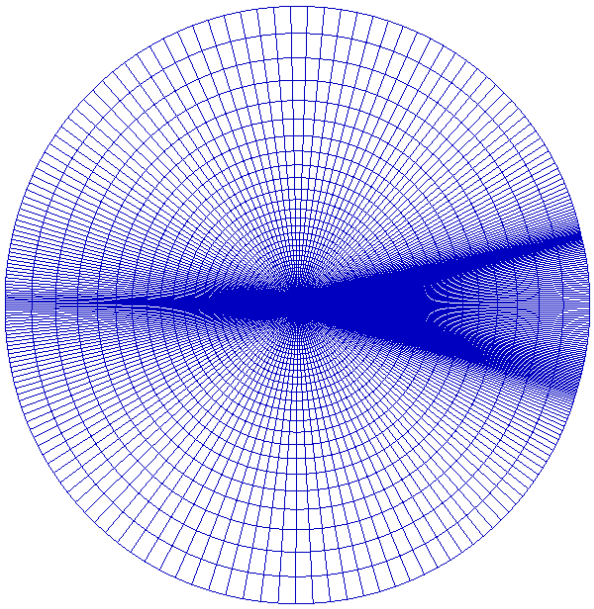

Figure 4.1: O-grid

4.4 Validation

A computational set-up able to capture the aerodynamics of the involved airfoils needs to be researched. In order to assess the reliability and hence the suitability of the numerical results obtained with the various set-ups, these will be judged in terms of:

- C_l and C_d values
- Pressure Coefficient (C_p) distributions
- Time histories
- Flow phenomena captured
- Strouhal number (St), based on the lift coefficient spectrum and using the TE height as reference length.

Where possible, the numerical results will be compared to the available experimental data [7] [20] [5]. Furthermore, the numerical code RFOIL [36] will also be included in the assessment of the numerical set-up. RFOIL is a modified version of XFOIL [37], able to calculate the effect of rotation on airfoil performance. It has proven to accurately predict the lift and drag coefficients for a variety of airfoils and flow conditions while keeping really low the computational costs.
As already mentioned, in this study, different numerical approaches with different fidelity levels are investigated. The comparison with RFOIL will not allow to evaluate the model in terms of numerical accuracy but also in terms of computational time. In other words, RFOIL will be the base for the judgement of the set-up efficiency.

4.5 Workflow

The workflow followed in this project derives directly from the objectives stated in Chapter 3 and is based on the outcomes of each step. This is schematically displayed in Figure 4.2: next to each objective, the type of simulations (test case) performed to achieve it are shown. The outcome deriving from each objective is used in the successive one. The details of each test case will be given in the Results Chapter 5, where a similar labelling is followed.

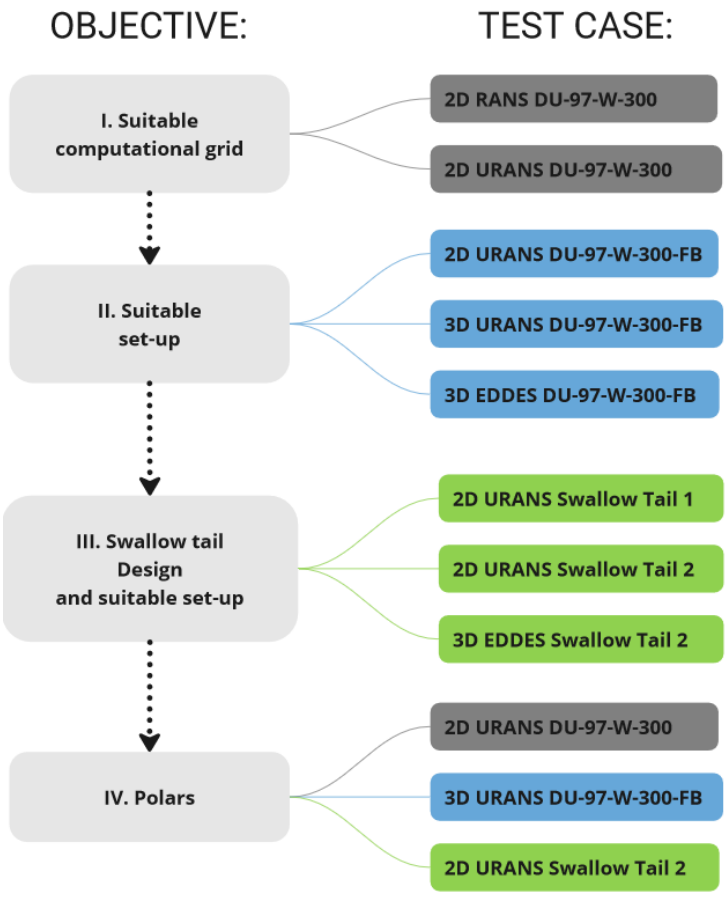

Figure 4.2: Workflow overview

5 Results

In this chapter, the results obtained throughout this research are shown. Each simulation case is sub-dived with a test case description, mesh and boundary conditions, the results and the deriving conclusions to be used in the successive test cases. All the simulations are performed with the general simulation set-up given in 4.2 unless differently specified.

5.1 2D RANS and 2D URANS DU97-W-300

5.1.1 Test case description

In the research of a suitable computational grid, a grid refinement and time refinement study has been carried out on the regular airfoil DU-97-W-300 using 2D RANS and 2D URANS respectively.

For this airfoil, the available experimental data at $Re = 1.6 \times 10^6$ include C_l values and C_p distributions under clean conditions for $\alpha = 11.9°$. However, for the research of a suitable grid, a lower angle of attack is chosen being this flow condition more steady and suitable for a grid refinement study. The obtained results will be compared to the experimental data available for $Re = 3 \times 10^6$. For the time refinement, the simulations are performed at higher angle of attack, being this flow condition more unsteady.

5.1.2 Mesh and Boundary Conditions

A structured O-mesh with a circular domain located approximately 140 chord lengths away is used.

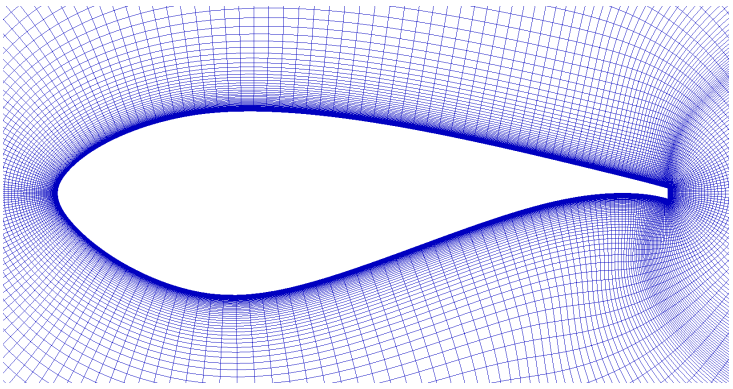

Figure 5.1: Near-body mesh DU97-W-300

Three grids with different number of nodes around the airfoil surface have been tested in this test case: 128, 258, 516. In Figure 5.1, the mesh with 258 nodes is shown. For all grids, the initial cell height is set to achieve a $y+$ value of 1 and a grow rate of 1.1 is used in the entire domain. This resulted in approximately 30 thousand cells (for the 258 grid).

On the circular domain the farfield boundary condition is applied which is used to denote the free-stream conditions. A no-slip adiabatic wall BC at the airfoil boundary is used.

5.1.3 Results

The first set of simulations are 2D RANS, which are performed on three grids having 128,258 and 516 nodes around the airfoil surface. The results in terms of C_l and C_d are given in Table 5.1. Being the results almost unvaried between grid 258 and 516, the grid selected for the successive investigations is the 258 one.

Grid	α [deg]	C_l	C_d
128	4	0.71	0.0199
258	4	0.70	0.0185
516	4	0.70	0.0183
experiments tripped $Re = 3 \times 10^6$	4.1	**0.72**	**0.0170**
RFOIL	4	0.74	0.0184

Table 5.1: Grid refinement study using 2D RANS on the regular DU97-W-300, $Re = 1.6 \times 10^6$.

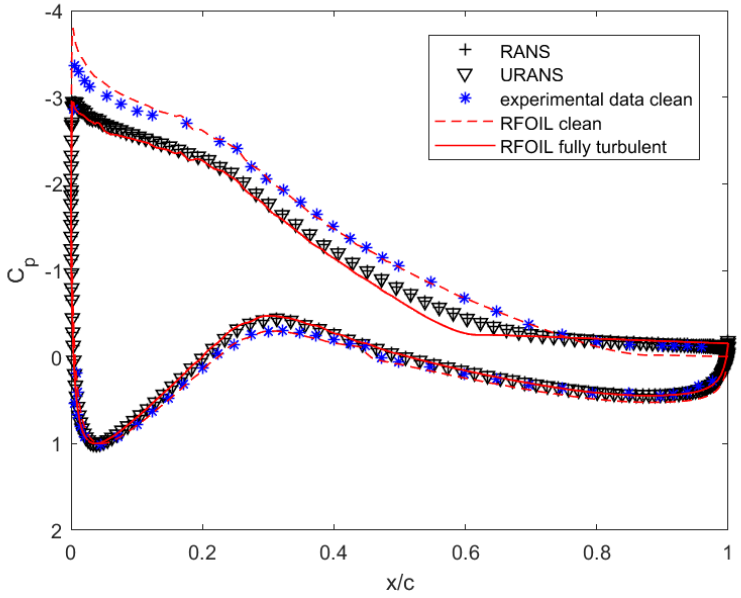

Figure 5.2: C_p distributions with different fidelity levels DU97-W-300, $Re = 1.6 \times 10^6$, $\alpha = 11.9°$

With regard to the 2D URANS simulations, the time refinement results obtained with the grid 258 were the same for all the time steps both in terms of aerodynamic coefficients and C_p distributions. This suggests that the flow around this airfoil does not have large unsteadiness. This can be seen in Figure 5.2, where the C_p distributions obtained with different methods are compared to the experiments. Indeed the RANS results overlap with the URANS ones. The clean RFOIL predictions are in good agreement with the clean experimental data, proving the high numerical accuracy of this code. RFOIL has indeed shown to be a reliable tool for the prediction of flow around thick airfoils [38]. Finally, the turbulent RFOIL results also match the SU2 ones for most of the airfoil surface.

Flow solution

In Figure 5.3, the velocity contour of the DU97-W-300 obtained with 2D URANS is displayed. It can be seen that, as expected, the flow separation on the suction side starts very early, right after the maximum thickness.

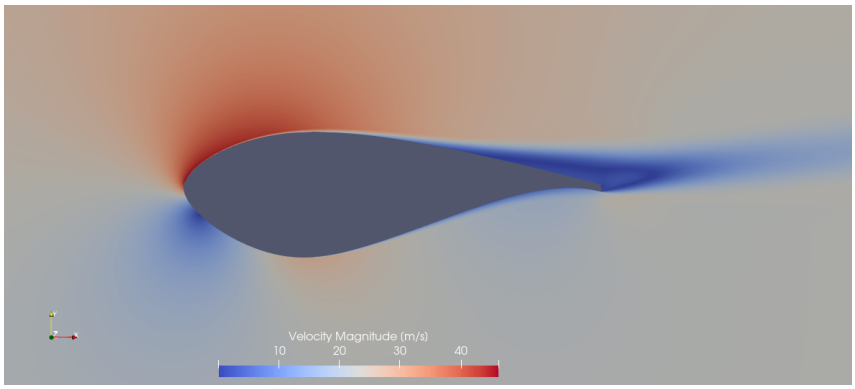

Figure 5.3: Velocity Contour 2D URANS DU97-W-300, $Re = 1.6 \times 10^6$, $\alpha = 11.9°$

5.1.4 Conclusions

Based on these results, the grid with 258 nodes around the airfoil is chosen for further analysis of both the regular and flatback airfoils. Furthermore, being the URANS and RANS results the same, it suggests that the flow around the regular airfoil does not have large unsteadiness. For such a flow, looking at Figure 5.2, RFOIL is the most suitable numerical approach in terms of accuracy/computational time.

5.2 2D URANS DU97-W-300-FB

5.2.1 Test case description

In the research of a suitable set-up for the prediction of the flow around flatback airfoils, the first set of simulations that has been performed is 2D URANS. In this set, two turbulence models, SST and SA, have been employed and a time refinement study carried out for each of them. Being the flow highly unsteady, as mentioned in Section 2.3, the RANS approach is unable to represent the physics of the involved flow and hence not considered at all in this test case.

For this airfoil, the available experimental data at $Re = 1.6 \times 10^6$ include C_l values and C_p distributions for tripped conditions at two angles of attack ($\alpha = 4.4$ and $\alpha = 11.6°$), C_l and C_d values for clean conditions at angle of attack $\alpha = 11.6°$. Finally, the Strouhal number, based on the trailing edge thickness, is available for tripped conditions at $\alpha = 11.6°$. However, its analysis will be covered in the comparison between 2D URANS and 3D EDDES simulations in 5.3.4.

5.2.2 Mesh and Boundary Conditions

A structured O-mesh with a circular domain located approximately 150 chord lengths away is used. Based on the grid refinement study given in 5.1.3, the grid has 258 nodes around the airfoil surfaces. In order to have a smooth match between the cells on the suction and pressure side of the airfoil and the ones at the TE, the optimal number of nodes at the TE resulted to be 100. This can be seen in Figure 5.4b, where the the cell length in the chord-wise direction (”Length, I”) in the boundary layer mesh is examined. It can be seen that the cell length does not change abruptly, but there is instead a smooth transition. The cell length in the normal direction is dictated by the initial cell height and grow rate. Also for this case, the initial cell height is set

to achieve a $y+$ value of 1 and a grow rate of 1.1 is used for the extrusion of both the boundary layer and the rest of the domain meshes. This resulted in approximately 52 thousand cells.

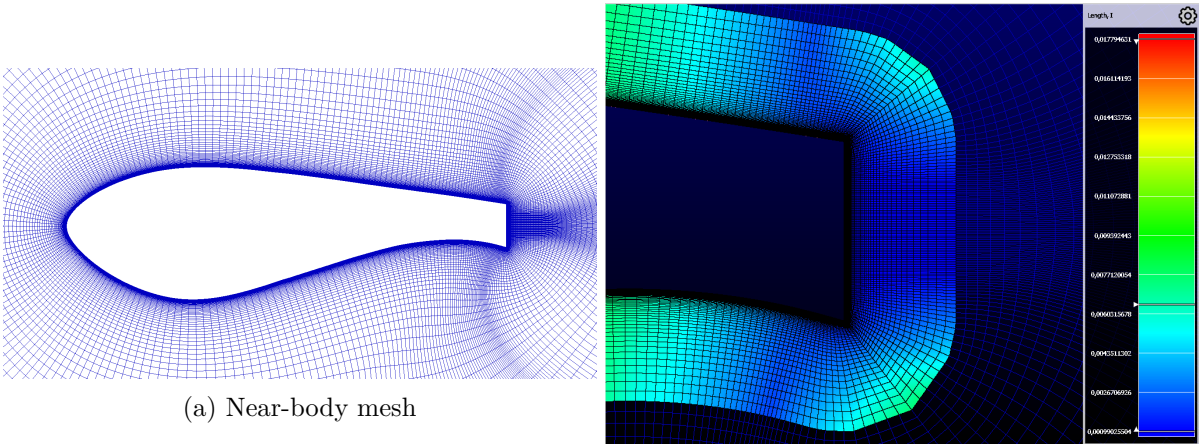

(a) Near-body mesh

(b) Chord-wise length of the cells around the TE

Figure 5.4: Near-body mesh DU97-W-300-FB

On the circular domain the farfield boundary condition is applied which is used to denote the free-stream conditions. A no-slip adiabatic wall BC at the airfoil boundary is used.

5.2.3 Results

The results have been first evaluated looking at the C_l and C_d values and correlated to the pressure distributions.
At low angle of attack, the C_l values between the two turbulence models were close to each other for all the time steps involved, while the C_d values resulted to be much higher for the SA model, especially at smaller time steps. At high angle of attack, larger values of both C_l and C_d were predicted with the SA model. Overall, as expected, the SST model predictions were closer to the experimental data.
The pressure distributions obtained with the two turbulence models overlap with each other for both angles of attack and resulted to be quite close to the experiments. This means that the difference in the prediction of the aerodynamic coefficients between the two models mainly derives from the wake modelling, where the larger separation occurs. This might explain the better performance of the SST model, which will then be the model used for subsequent simulations.

The time refinement results obtained with the SST model are shown in Table 5.2.

Time step [sec]	α [deg]	C_l	C_d	α [deg]	C_l	C_d
$dt = 0.00015$	4.4	0.87	0.0718	11.6	1.73	0.0569
$dt = 0.0003$	4.4	0.87	0.0679	11.6	1.75	0.0594
$dt = 0.0006$	4.4	0.86	0.0668	11.6	1.75	0.0611
experiments tripped	4.4	**0.83**	–	11.6	**1.74**	**-**
experiments clean	–	–	–	11.6	**1.94**	**0.0509**

Table 5.2: Time refinement study using 2D URANS SST on the DU97-W-300-FB, $Re = 1.6\times10^6$, $\alpha = 4.4$ and $\alpha = 11.6$,

At low angle of attack, the C_l values are the same for $dt = 0.00015$ and $dt = 0.0003$. At larger angle, the obtained C_l values differ of only 0.01%. Furthermore the C_l experimental value is an average of the two. Hence, following an engineering approach, the time step $dt = 0.0003$ is

considered a good compromise between accuracy and computational time. This will be used in the successive 2D URANS simulations.

Flow solution

In Figure 5.5, the velocity contours of the DU97-W-300-FB obtained with 2D URANS SST for two angles of attack are displayed. Similar results were obtained with the SA model. It can be seen that, as expected, the flow separation on the suction side is delayed compared to the regular airfoil. On the other hand, in the wake it is visible the presence of vortex shedding, not present in the regular airfoil.

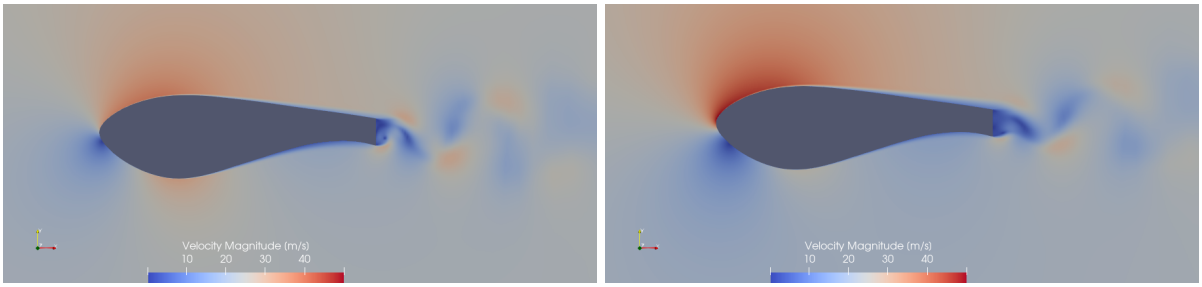

(a) $\alpha = 4.4°$ (b) $\alpha = 11.6°$

Figure 5.5: Velocity Contour 2D URANS DU97-W-300 -FB, $Re = 1.6 \times 10^6$

5.2.4 Conclusions

From the above analysis, the flow around the flatback airfoil consists of a delayed separation compared to the regular airfoil and an unsteady wake characterized by alternating vortices. The most suitable set-up for the prediction of such a flow using the 2D URANS approach, includes the SST turbulence model and a time step $dt = 0.0003$. In the upcoming sections, the displayed 2D URANS results refer to these settings which will also be applied to conduct successive 2D URANS simulations.

5.3 3D URANS and 3D EDDES DU97-W-300-FB

5.3.1 Test case description

In the research of a suitable set-up for the prediction of the flow around flatback airfoils, the second set of simulations employs higher fidelity approaches, namely 3D URANS and 3D EDDES. In this set, two spanwise sizes of the domain are tested: one extending to 5 chord lengths (SW5) and one extending to 2 chord lengths (SW2). Since EDDES simulations are embedded only with the SA turbulence model, this one has been used for all the 3D cases.
To enable a faster convergence, the EDDES simulations are carried out using as input the URANS solution. In particular, the simulation procedure consists of the following steps:

1. It is first tried to obtain a converged URANS solution.
2. This solution is used as initial condition for the EDDES simulation

The URANS solution to be given as input to the EDDES does not need to be fully converged. A non converged solution can actually result to be beneficial as it will be shown in the results, especially concerning the SW2 case.
The available experimental data are the same as given in Section 5.2.1. However, most of the results are obtained only for the higher angle of attack $\alpha = 11.6°$. In particular 3D EDDES with SW5 are available for both angle of attack while 3D URANS simulations are available only for

$\alpha = 11.6°$. This because based on the several trials performed for this angle of attack, as it will be shown in the results, 3D URANS is not suitable for the prediction of flow around the flatback airfoil. For the same reason, 3D URANS SW2 simulations are available only for $\alpha = 11.6°$ while 3D EDDES SW2 are available only for this angle because of time constrains.

5.3.2 Mesh and Boundary Conditions

Two 3D meshes with a circular domain are tested: one with spanwise extension of 5c (Figure 5.6a) and one 2c (Figure 5.6b). The initial cell height is set to achieve a $y+$ value of 1. Given the higher refinement required by the EDDES simulation, a grow rate of 1.05 is used for the near airfoil region and a value of 1.08 towards the farfield. This increases further the computational time. For this reason the domain for the 3D simulations is smaller than the 2D cases. In particular, for the SW5 the domain is located approximately 100 chords away, resulting in approximately 8 million cells. For the SW2, given the large simulation time observed with the SW5, the domain is reduced even further: from 100c to approximately 75c.

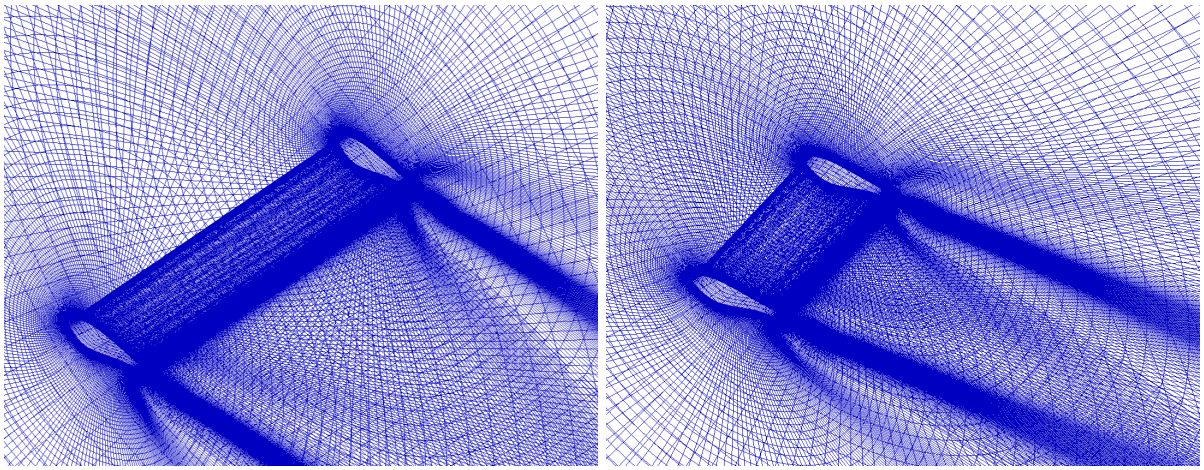

(a) SW5 (b) SW2

Figure 5.6: Near-body 3D Mesh DU97-W-300-FB

On the circular domain the farfield boundary condition is applied which is used to denote the free-stream conditions. A no-slip adiabatic wall BC at the airfoil boundary is used. Periodic boundary conditions were imposed on both the spanwise faces, meaning that an ”infinite” wing is resembled.

5.3.3 Results 3D URANS vs 3D EDDES SW5 and SW2

The results have been first analyzed looking at the C_l and C_d values and the C_l and C_d time histories. Looking at Table 5.3, at low AoA the EDDES prediction of the lift coefficient is quite close to the experimental value, while at high AoA, the lift resulted to be under-predicted by the URANS and over-predicted by the EDDES. However, it must be noted that the reported values are averaged ones.
Looking at the time histories in Figure 5.7, the C_l values for the EDDES cases present larger oscillations than the URANS ones, especially for the reduced spanwise case. This is indeed what it is expected for a flow characterized by high unsteadiness. The larger oscillations for the EDDES SW2 case will also be reflected in the Strouhal number, as it will be shown in 5.3.4. This, however, does not affect the C_l and C_d values, which resulted to be the same for both the SW2 and SW5 cases.

Method	α [deg]	C_l	C_d	α [deg]	C_l	C_d
3D URANS SW5	4.4	–	–	11.6	1.69	0.0408
3D URANS SW2	4.4	–	–	11.6	1.68	0.0404
3D EDDES SW5	4.4	0.85	0.0634	11.6	1.80	0.0674
3D EDDES SW2	4.4	–	–	11.6	1.80	0.0685
experiments tripped	4.4	**0.83**	–	11.6	**1.74**	–
experiments clean	–	–	–	11.6	**1.94**	**0.0509**

Table 5.3: 3D URANS and 3D EDDES with different spanwise extensions DU97-W-300-FB vs experiments, $Re = 1.6 \times 10^6$, $\alpha = 4.4°$ and $\alpha = 11.6°$

What is noticeable is that the URANS simulations predict a much smaller drag coefficient. This can be explained by looking at these less oscillating time histories and the C_p plots and the flow solutions given in the next section.

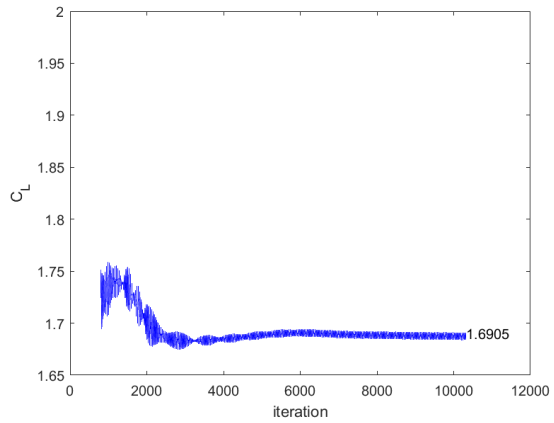

(a) 3D URANS SW5

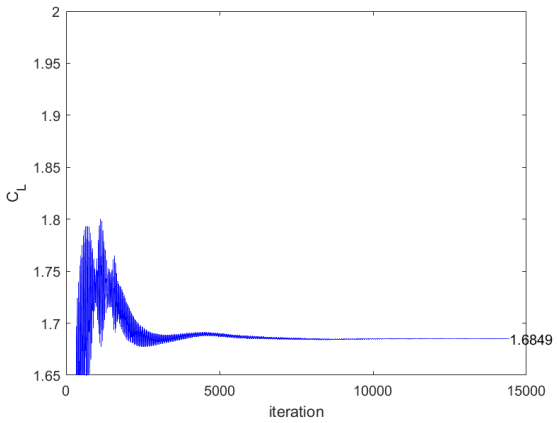

(b) 3D URANS SW2

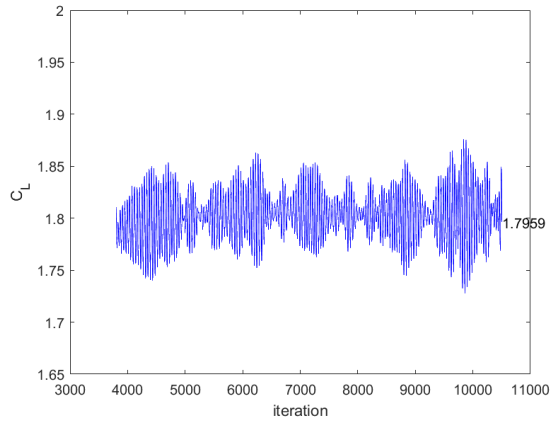

(c) 3D EDDES SW5

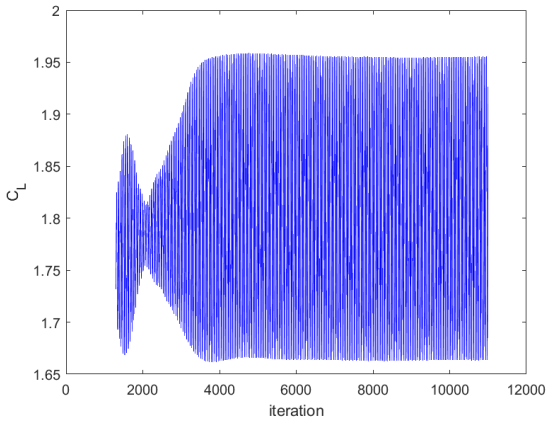

(d) 3D EDDES SW2

Figure 5.7: C_l time histories, 3D URANS and EDDES DU97-W-300-FB, $Re = 1.6 \times 10^6$, $\alpha = 11.6°$

Flow Solution

In the literature review it has been stated that the main contribution to the drag in flatback airfoils is due to the base drag, which can be visualized with a lowering of the pressure behind the trailing edge. Looking at the C_p plots in Figure 5.8b, it can be seen that 3D URANS fails in

the prediction of the low pressure behind the trailing edge and hence estimates a lower C_d. On the other hand, the C_p obtained with EDDES follows the experimental data. The capability of EDDES in predicting the vortex shedding, which is formed due to this low pressure, can also be visualized in the C_p contours in Figure 5.8d.

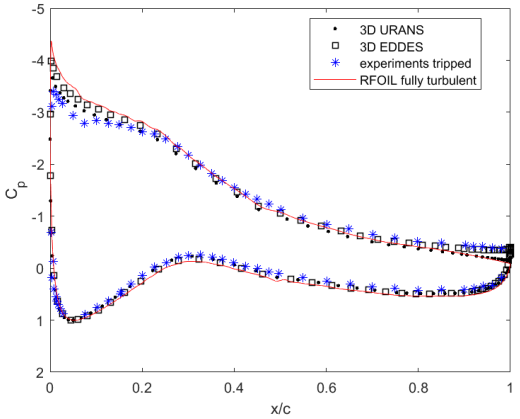

(a) C_p plots

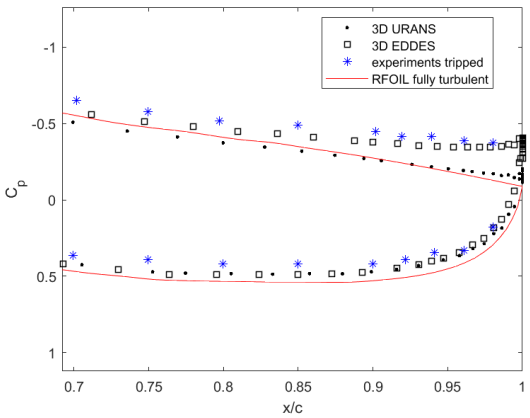

(b) C_p plots, zoom TE

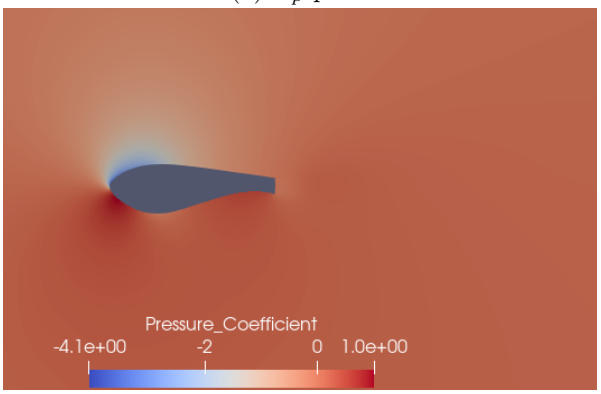

(c) C_p contour 3D URANS

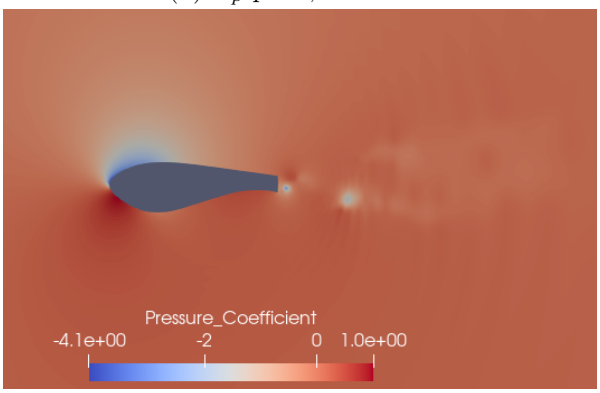

(d) C_p contour EDDES

Figure 5.8: C_p predictions 3D URANS (SW2) vs 3D EDDES (SW2) DU97-W-300-FB, $Re = 1.6 \times 10^6$, $\alpha = 11.6°$

Furthermore, in Figure 5.9, the turbulent eddy viscosity predictions are displayed. It can be seen that for the EDDES simulations, the eddy viscosity is much lower. This is because EDDES resolves the eddies while URANS models them. The dissipative behaviour of URANS approach can also be seen by comparing the results at the beginning (Figures 5.9a and 5.10a) and the end of the simulations (Figures 5.9b and 5.10b): the more the solution converges, the more the unsteadiness of the flow is neglected. For this reason, it is better to initialize the EDDES simulation with a non converged URANS solution. This also explains the smaller oscillations of the C_l time history for the URANS cases.

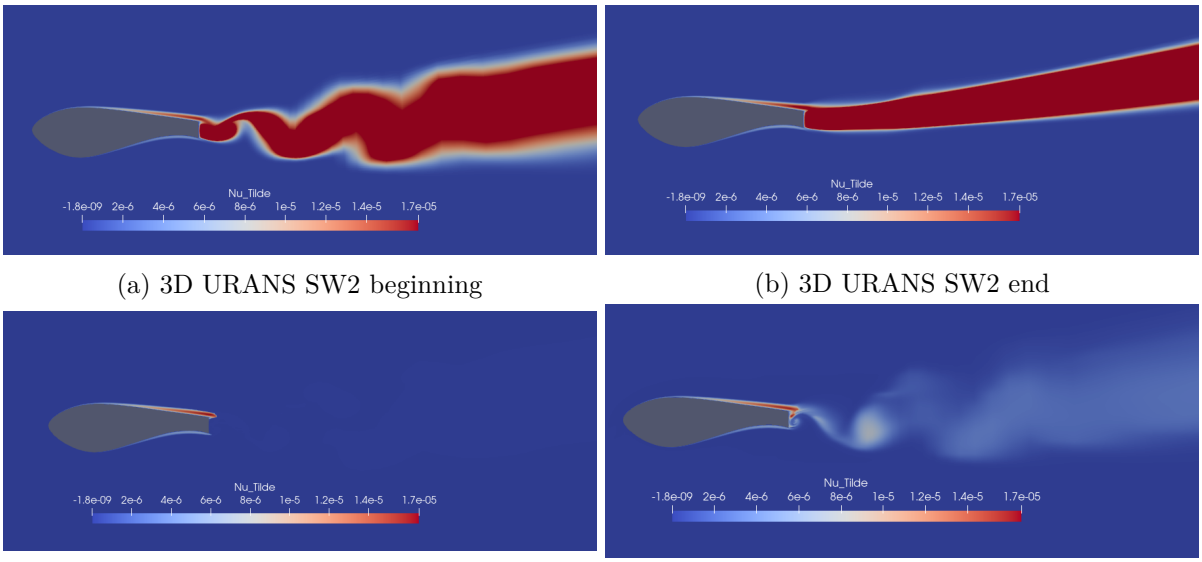

(a) 3D URANS SW2 beginning

(b) 3D URANS SW2 end

(c) 3D EDDES SW2 end

(d) 3D EDDES SW5 end

Figure 5.9: Turbulent eddy viscosity contours 3D URANS and EDDES DU97-W-300-FB, $Re = 1.6 \times 10^6$,$\alpha = 11.6°$

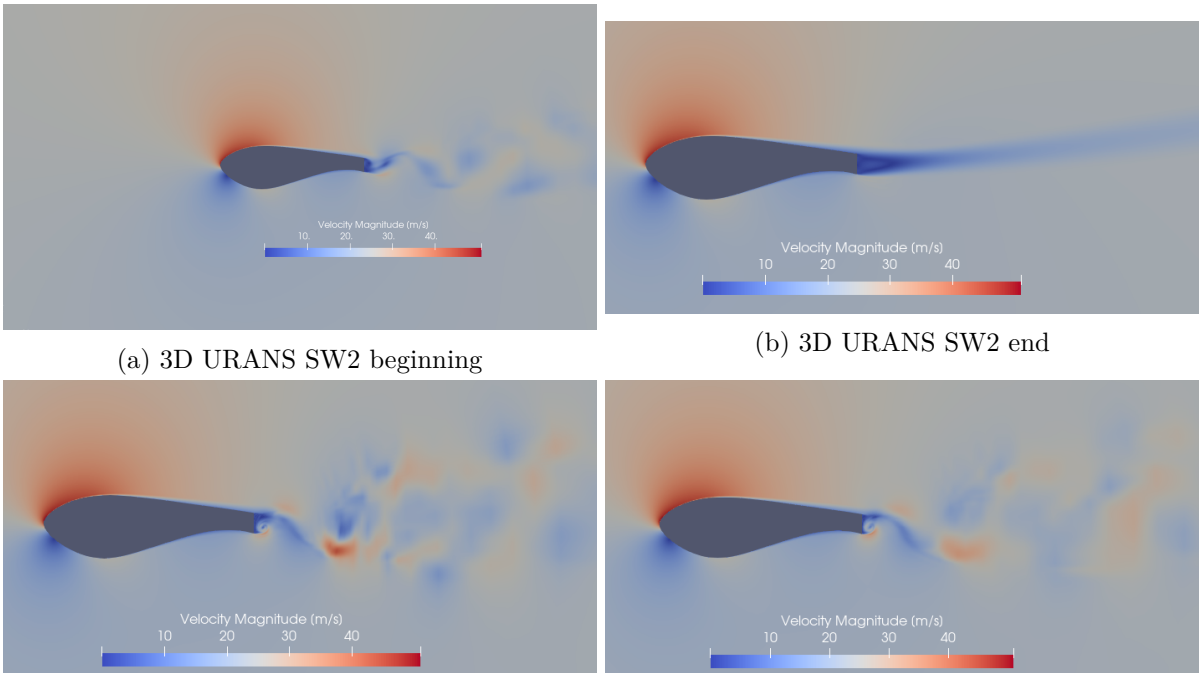

(a) 3D URANS SW2 beginning

(b) 3D URANS SW2 end

(c) 3D EDDES SW2 end

(d) 3D EDDES SW5 end

Figure 5.10: Velocity Contours 3D URANS and EDDES DU97-W-300-FB, $Re = 1.6 \times 10^6$, $\alpha = 11.6°$

Finally it can be seen that the EDDES approach achieves good performances with both the SW2 and SW5 spanwise extension: the vortex shedding is present in both cases Figure 5.10c and 5.10d.
It can be concluded that 3D URANS is not suitable for the prediction of the flow around flatback airfoils and hence, this approach will not be considered in any subsequent investigation. With regard to the spanwise extension, a spanwise $2c$ provides the same results of a spanwise $5c$. Furthermore, the computation time of SW2 is much lower than the one with SW5. Hence, the

following EDDES simulation performed in this study will be done with SW2 (Section 5.5).

5.3.4 Results 2D URANS vs 3D EDDES

In order to understand which fidelity level is more suitable for the prediction of the flow around the flatback airfoil DU97-W-300-FB, the numerical results obtained with 2D URANS and 3D EDDES will be compared. RFOIL predictions will also be included while, as concluded in 5.3.3, 3D URANS will not be considered.
The results will be evaluated in terms of aerodynamic coefficients, pressure coefficient distributions, Strouhal number and flow solutions for two angles of attack. Since the 3D EDDES SW2 simulation has been carried out only for $\alpha = 11.6°$, in this section the 3D EDDES SW5 results will be reported for the comparison. However, it is important to keep in mind that the 3D EDDES SW2 predictions resulted to overlap with the ones obtained with the SW5.

The aerodynamic coefficients, together with the Strouhal number, are given in Table 5.4. At low AoA, the C_l coefficient predicted with EDDES is closer to the experimental value than the URANS one. At higher AoA, the opposite is true. However, as previously stated it must be remembered that this are average values and that, being the flow highly unsteady, also the experimental data must be considered with this precaution.
With respect to the C_d, the difference between URANS and EDDES is larger at higher AoA, with a smaller C_d predicted by the URANS. This might be due, again, to the fact that URANS fails in predicting the base drag. Indeed URANS only models the large eddies while EDDES resolves them: at higher angle of attack the wake might be constituted by larger eddies due to the formation of a lower pressure zone behind the trailing edge. This is confirmed by looking at the C_p plots in Figure 5.11 and the flow solution in Figure 5.13. At low angle of attack, the C_p plots obtained with the two approaches follow quite accurately the experimental data, where also the low pressure at the TE is well captured. On the other hand, at higher AoA towards the TE, the URANS result moves away from the experimental data, while the EDDES remains close to it (Figure 5.11d).

Method	α [deg]	C_l	C_d	St	α [deg]	C_l	C_d	St
2D URANS	4.4	0.87	0.0680	0.17	11.6	1.75	0.0594	0.17
3D EDDES	4.4	0.85	0.0634	0.12	11.6	1.80	0.0674	0.12
RFOIL	4.4	0.96	0.0310	–	11.6	1.86	0.0372	–
experiments tripped	4.4	**0.83**	–	≈ 0.24	11.6	**1.74**	–	≈ 0.24
experiments clean	–	–	–	–	11.6	**1.94**	**0.0509**	–

Table 5.4: Numerical results for the DU97-W-300-FB with different fidelity level vs experiments, $Re = 1.6 \times 10^6$, $\alpha = 4.4$ and $\alpha = 11.6$,

Finally, it is interesting to see how the RFOIL predictions are not as close to the experimental data and SU2 results as for the regular airfoil. Looking at the C_p distributions, they basically overlap with the EDDES predictions for both the AoA here evaluated. However, towards the trailing edge, the accuracy drops.
Regarding the Strouhal number, it can be seen that there is a large difference between the numerical results and the experimental values. What has been noticed is that when the Strouhal number, defined as $St = f_s L/U_\infty$, was computed using the chord c as reference length L instead of the TE height h, the EDDES results overlapped with the experimental ones. In particular, the St computed with 2D URANS and 3D EDDES was $St = 0.33$ and $St = 0.25$ respectively. On the one hand, it must be noted that this experimental data are based on averaged acoustic spectra. On the other hand, in other studies (i.e. [14]) in which the St was also computed based on the C_L spectrum and h, a $St \approx 0.21$ was obtained. It is then unclear why the numerical results obtained

with both EDDES and URANS do not match the values found in the literature. However, as in the experiments, the St does not change with angle of attack. Finally, in Figure 5.12, it can be seen that the St obtained with EDDES with a smaller spanwise extension (SW2) is the same as the one with the larger one (SW5), $St = 0.12$. The only difference is the amplitude at which this vortex shedding occurs. Here the amplitude of the power spectral density (PSD) is normalized with the largest present peak (in this case the SW2). In this way it can be seen that for SW2 the amplitude is about 140% larger. This might explain the difference in turbulence eddy viscosity between SW2 (Figure 5.9c) and SW5 (Figure 5.9d).

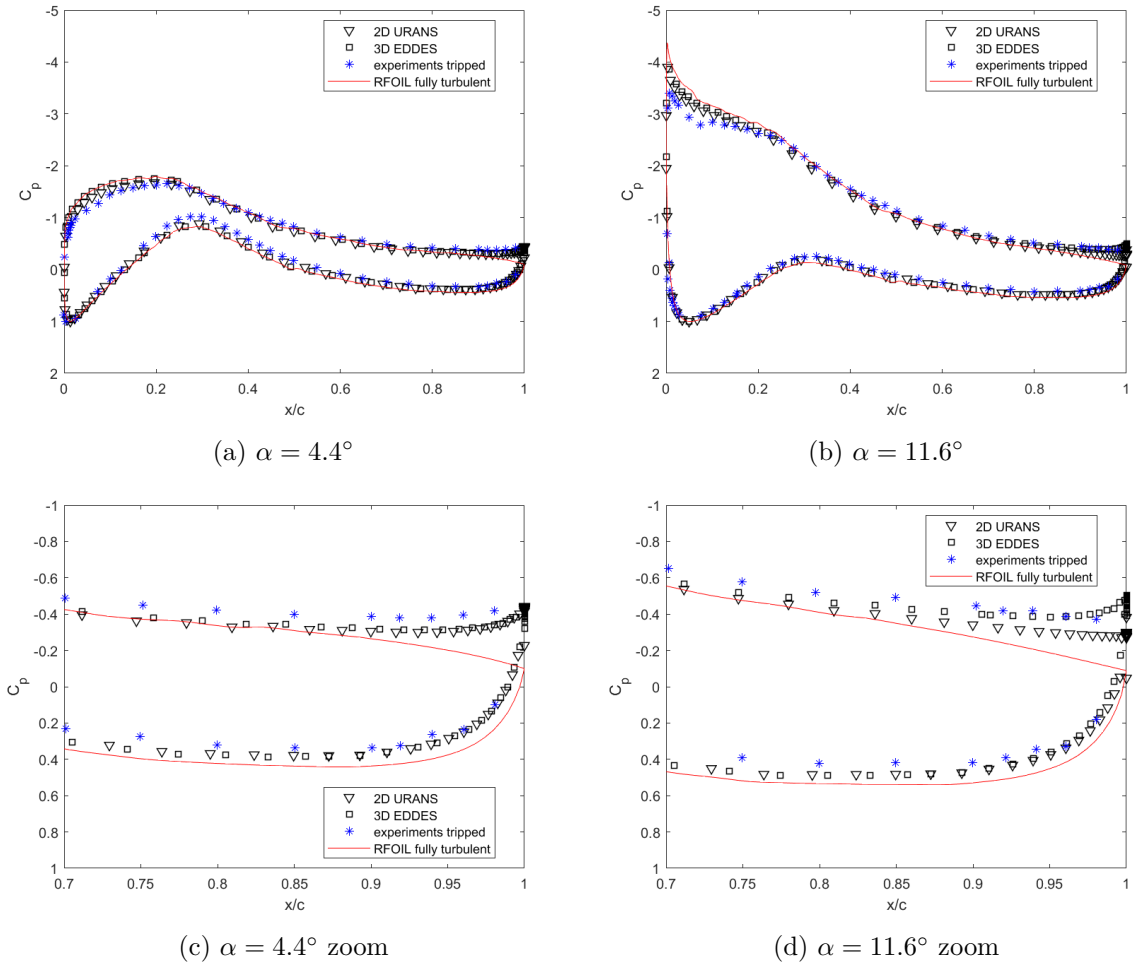

(a) $\alpha = 4.4°$

(b) $\alpha = 11.6°$

(c) $\alpha = 4.4°$ zoom

(d) $\alpha = 11.6°$ zoom

Figure 5.11: Pressure Distributions DU97-W-300-FB with different fidelity levels, $Re = 1.6 \times 10^6$

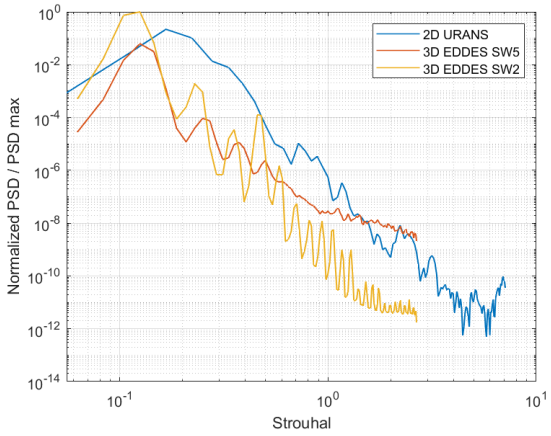

Figure 5.12: Frequency spectrum based on the C_l time series with different fidelity levels for the DU97-W-300-FB, $Re = 1.6 \times 10^6$, $\alpha = 11.9°$

Flow Solution

From the pressure contours, displayed in Figure 5.13, it can be seen that both URANS and EDDES are able to predict the pressure drop behind the trailing edge. It is interesting to note that 2D URANS gives a better prediction than 3D URANS. This can be due to the fact that 2D URANS simulations are carried out with the SST turbulence model, which is known to perform better in separated flow compared to the SA model used in the 3D URANS simulations. However, the good performance of the 2D URANS remains limited to low AoA. Indeed, the accuracy drops with increasing AoA. This can also be visualised by looking at the velocity contours in 5.14, where the wake predicted by the EDDES is much more unsteady than the one obtained with URANS.

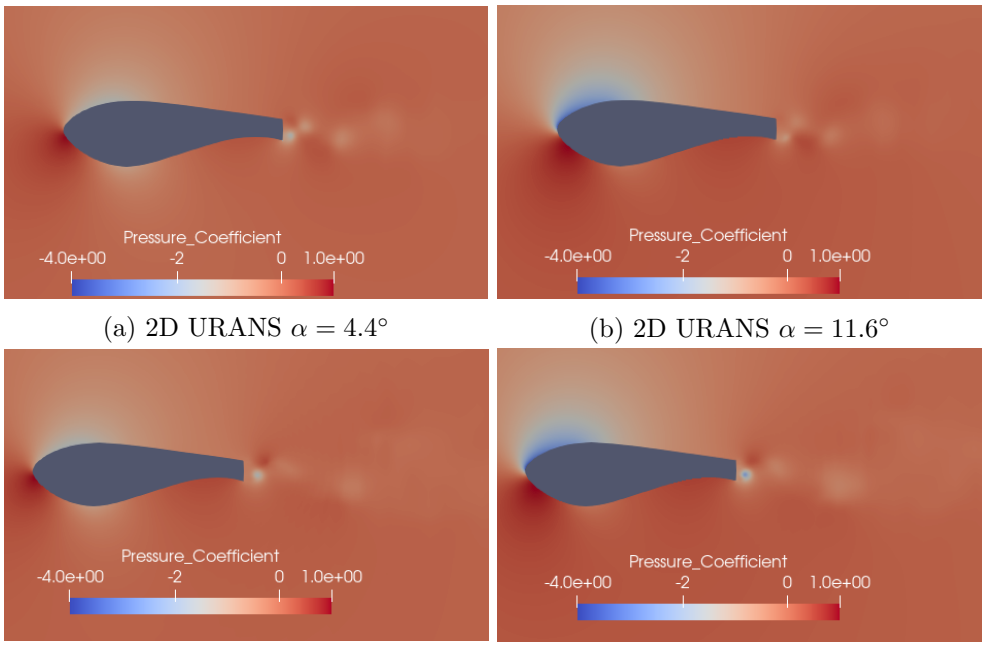

(a) 2D URANS $\alpha = 4.4°$

(b) 2D URANS $\alpha = 11.6°$

(c) 3D EDDES$\alpha = 4.4°$

(d) 3D EDDES $\alpha = 11.6°$

Figure 5.13: C_p Contours DU97-W-300-FB with different fidelity levels, $Re = 1.6 \times 10^6$

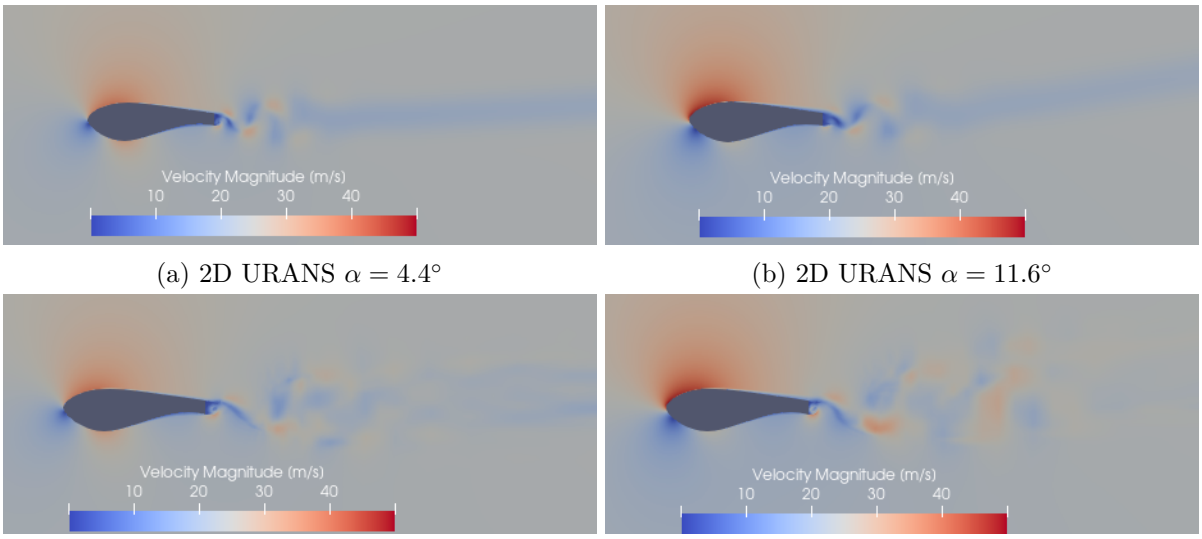

(a) 2D URANS $\alpha = 4.4°$ (b) 2D URANS $\alpha = 11.6°$

(c) 3D EDDES $\alpha = 4.4°$ (d) 3D EDDES $\alpha = 11.6°$

Figure 5.14: Velocity Contours DU97-W-300-FB with different fidelity levels, $Re = 1.6 \times 10^6$

5.3.5 Conclusions

From the above analysis, the most suitable fidelity level for the prediction of the flow around flatback airfoil is the 3D EDDES. However, if the computational time is included, 2 URANS results to be the most efficient method.
Indeed the 2D URANS approach, being embedded with SST turbulence model, also provided mean C_l and C_d values and pressure distributions that are close to the experimental bounds and better than the 3D URANS results. However, this accuracy drops at higher AoA, where the wake is constituted by larger eddies. In particular, in order to fully capture the vortex shedding phenomena, accurate predictions of the pressure drop behind the trailing is primarily important. This is then achieved with the EDDES simulations. Both the EDDES SW2 and SW5 were able to capture this phenomena but, given the lower computational time of the SW2, this will be chosen for future EDDES simulations.

5.4 2D URANS Swallow Tail Designs

5.4.1 Test case description

In Section 5.2 it has been shown that the set-up 2D URANS in combination with the SST turbulence model is capable of capturing the main flow phenomena involved around flatback airfoils and accurately predicting the aerodynamic coefficients. Hence, this set-up is used in the evaluation of the designed swallow tail concepts. Two designs have been proposed:

1. Swallow Tail 1 (ST1), which develops from the general indications given in the patent application [10]
2. Swallow Tail 2 (ST2), which develops from the numerical analysis performed on ST1.

The details of each design are given in the following sections.

Finally, the purpose of the swallow tail design is to reduce the drag of the flatback airfoil while maintaining its advantages. Since for $Re = 1.6 \times 10^6$ it has been shown that the FB seems to have larger eddies at angle of attack $\alpha = 11.6$, the aerodynamic investigations of the proposed concepts will be performed at these flow conditions.

Swallow Tail 1

The first proposed design has as starting geometry the DU-97-W-300-FB and develops the swallow tail from the general indications given in the patent application [10], in particular:

- Cut off the pressure side curve of approximately 10%c
- Create a non-symmetrical cavity

These features should suppress the coupling between the vortices generating from the pressure and suction sides.
Furthermore, to have a more realistic design and have a geometry that can be meshed with the same mesh topology of the flatback, the swallow tail design will be free of any sharp edges. In particular:

- Finite trailing edge thickness, chosen to be equal to the t_{TE} of the regular airfoil.

The first swallow tail concept design is displayed in Figure 5.15. The angle β has been chosen large enough to create a non-symmetrical cavity but at the same to limit its concavity. The idea is to ensure that the flow from the lower side separates towards the upper one and does not recirculate within the cavity. Hence, another design indication is given:

- Limited cavity concavity

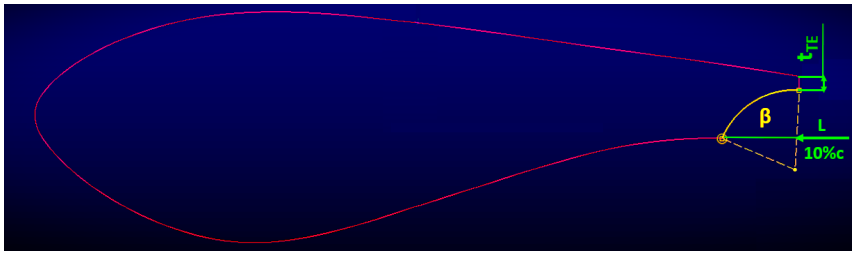

Figure 5.15: Swallow Tail 1 and Design Parameters

This first concept design highligts the parameter involved in the developing of a swallow tail geometry:

1. Trailing edge thickness t_{TE}
2. "Concavity" angle β
3. Length of pressure side cut-off L

Swallow Tail 2

The second proposed design is developed upon the numerical aerodynamic results of ST1. In particular, as it will be shown in the results section, the lift coefficient generated by the first design is much lower. Hence, to address this lift drop, the pressure side of ST2 is created longer than the one of ST1. In other words, the cut-off length L is shorter. This will indeed result in an increased lift coefficient.
The geometry can be visualized in Figure 5.16. The mesh and the boundary conditions are the same for both ST1 and ST2. Since ST2 will be the selected concept for further investigations, the grid generated for SW2 will be shown. In Table 5.5 the dimensions of the design parameters used for the two concepts are given.

Design	t_{TE}	β [deg]	L
ST1	$0.017c$	70	$0.101c$
ST2	$0.017c$	40	$0.049c$

Table 5.5: Swallow Tail design parameters

5.4.2 Mesh and Boundary Conditions

A structured O-mesh with a circular domain located approximately 100 chord lengths away is used and displayed in Figure 5.16. As for the flatback, the optimal number of nodes at the backside of the airfoil resulted to be 100: 35 at the TE and 65 at the curved side. The initial cell height is set to achieve a $y+$ value of 1. Since the same mesh will be extended in the spanwise direction for the performing of EDDES simulations, the grid is implemented with a resolution suitable for the EDDES case. Hence, a grow rate of 1.05 is used for the near airfoil region and a value of 1.08 towards the farfield. This resulted in approximately 81 thousand cells.

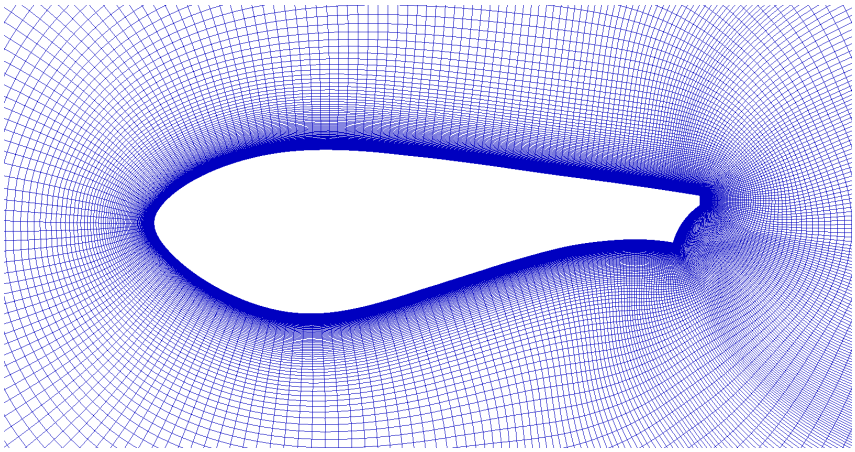

Figure 5.16: Near-body mesh Swallow Tail 2

On the circular domain the farfield boundary condition is applied which is used to denote the free-stream conditions. A no-slip adiabatic wall BC at the airfoil boundary is used.

5.4.3 Results

In order to check if the swallow tail improves the performance of the flatback, the results are first inspected in terms of aerodynamic coefficients, with particular attention to the lift to drag ratio (C_l/C_d). Subsequently, the flow characteristics will be analyzed and compared with the regular and flatback airfoils flow solutions.

In Table 5.6, it can be seen that the first swallow tail design already outperforms both the standard and the flatback airfoils in terms of efficiency: 51% lower drag resulting in a 41% higher C_l/C_d. However, this concept does not exploit the full potential of the flatback in terms of lift. For this reason, a second design has been proposed, ST2, where the pressure side is longer than the one of ST1. This results in a higher C_l and improved performance: efficiency increase of 43% compared to the FB and 26% compared to the regular airfoil. To put the results in perspective, the experimental data under clean conditions are also displayed (Table 5.6b) .

airfoil	α [deg]	C_l	C_d	C_l/C_d
regular	11.9	1.32	0.0397	33.37
FB	11.6	1.75	0.0594	29.40
ST1	11.6	1.19	0.0288	41.37
ST2	11.6	1.42	0.0337	42.09

(a) 2D URANS

airfoil	α [deg]	C_l	C_d	C_l/C_d
regular	11.9	1.57*	–	–
FB	11.6	1.94*	0.0509*	38.11*

(b) Experimental data *:clean

Table 5.6: Aerodynamic coefficients and efficiency for the regular, flatback and swallow tail airfoils, $Re = 1.6 \times 10^6$

A time refinement of the ST1 has also been performed. The results were the same for all the tested time steps, anticipating the lower unsteadiness of this geometry compared to the flatback. This was also reflected in the time history plots which resulted to be almost oscillations free for all the time steps.

Flow solution

From the velocity contours, displayed in Figure 5.17, it can be seen that the swallow tail retains the advantages of the flatback while reducing the drawbacks: the separation on the suction side is postponed and the wake unsteadiness reduced.

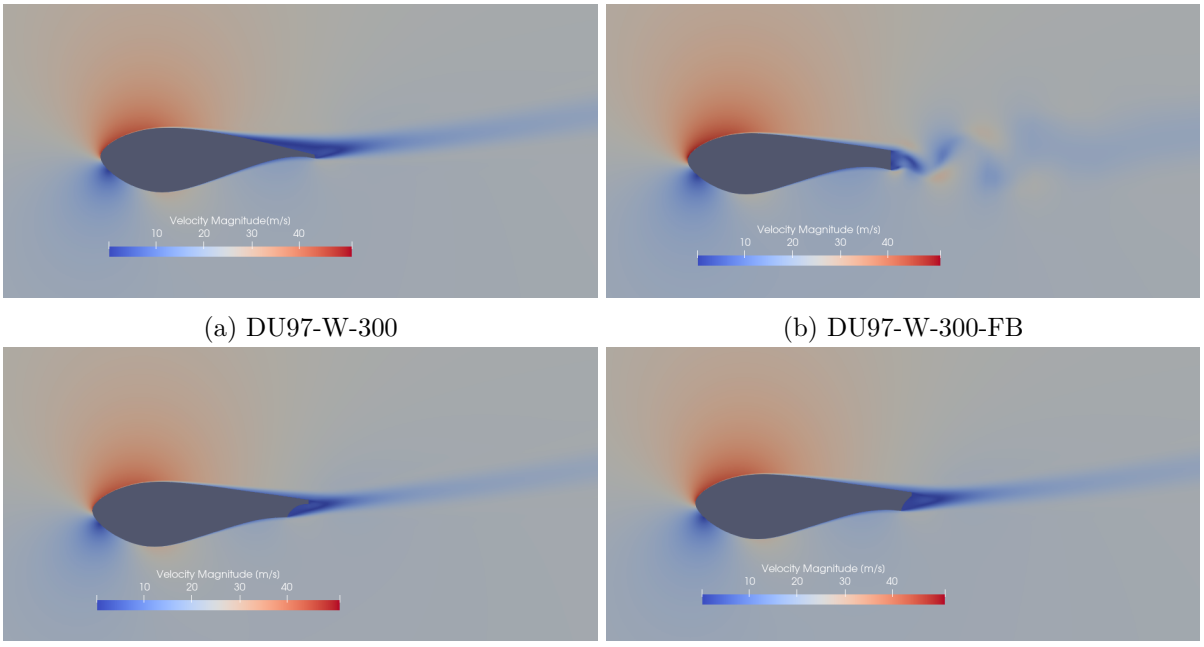

(a) DU97-W-300

(b) DU97-W-300-FB

(c) Swallow Tail 1

(d) Swallow Tail 2

Figure 5.17: Velocity Contours 2D URANS, $Re = 1.6 \times 10^6$

5.4.4 Conclusions and Considerations

The swallow tail design outperforms both the regular and the flatback airfoils. The ratio C_l/C_d resulted to be larger thanks to the postponed separation deriving from the reduced curvature near the trailing edge and the reduced unsteadiness obtained with the asymmetric cavity. An even improved performance is obtained by extending the pressure curve(ST2).

In order to verify the correctness of this outcome, an higher fidelity simulation with EDDES is performed on the ST2 and given in 5.5.

Furthermore, it must be observed that the comparison is made at one angle of attack and at $Re = 1.6 \times 10^6$. Looking at 5.18, this flow condition is probably disadvantageous for the regular airfoil: at $\alpha = 11.9$ it is likely to be in stall conditions. Hence, a comparison between the proposed concepts must be made on a range of angles of attack. Because of the larger availability of experimental data, this comparison will be made at $Re = 3 \times 10^6$ and given in 5.6.

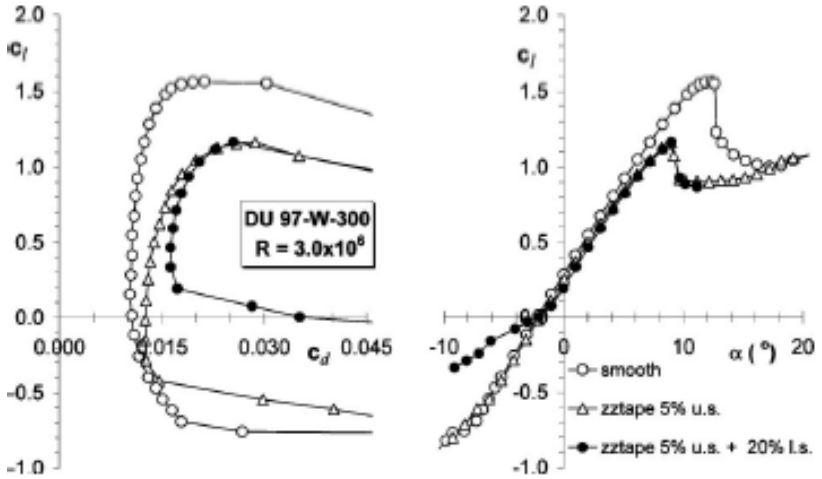

Figure 5.18: Experimental Data DU97-W-300 $Re = 3 \times 10^6$ [5]

5.5 3D EDDES Swallow Tail 2

5.5.1 Test case description

According to the 2D URANS simulations, the swallow tail design and, particularly, ST2, outperforms both the regular and flatback airfoils. In order to verify the correctness of this outcome, EDDES simulation will be performed and compared to the 2D URANS results. Hence, the flow conditions are $Re = 1.6 \times 10^6$ and $\alpha = 11.6°$.

5.5.2 Mesh and Boundary Conditions

The 3D mesh for this case is obtained by translating in the spanwise direction the same mesh used in the 2D simulations (5.4.2). In 5.3.3, it has been shown that a spanwise extending to 2 chord lengths (SW2) is sufficient to accurately capture the flow phenomena involved. Hence the spanwise of this case extends to $2c$. The same boundary conditions used for the 3D flatback case are applied (5.3.2).

5.5.3 Results 2D URANS vs 3D URANS ST2

The results obtained with the two different fidelity level approaches are first analyzed in terms of aerodynamic coefficients and Strouhal number. From Table 5.7, it can be seen that the swallow tail simulations performed with EDDES predicted a larger C_l and, particularly, C_d compared to the 2D URANS, resulting in a lower efficiency. However, the swallow tail concept still shows the highest C_l/C_d ratio amongst all the tested geometries both with the 2D URANS and EDDES approach. Indeed, even if the C_d of the swallow tail resulted to be larger, the drag reduction compared to the FB is still of 40%. The reason why the EDDES predicted a larger C_d can be explained by looking at the flow solution given in the next section.

airfoil	α [deg]	C_l	C_d	C_l/C_d
regular	11.9	1.32	0.0397	**33.37**
FB	11.6	1.75	0.0594	**29.40**
ST2	11.6	1.42	0.0337	**42.09**

(a) 2D URANS

airfoil	α [deg]	C_l	C_d	C_l/C_d
regular	11.9	–	–	–
FB	11.6	1.80	0.0685	**26.28**
ST2	11.6	1.49	0.0409	**36.43**

(b) 3D EDDES

Table 5.7: Aerodynamic coefficients and efficiency for the regular, flatback and swallow tail airfoils with different fidelity levels, $Re = 1.6 \times 10^6$

With respect to the Strouhal number, no peaks were observed in the frequency spectrum obtained with the 2D URANS simulations. This highlights the deficiencies of this approach in capturing the vortex shedding phenomena, as it will be shown in the flow solution. With respect to the EDDES solution, a $St = 0.18$ was predicted, resulting in an increased value compared to the flatback $St = 0.12$, as shown in Figure 5.19. Here the amplitude of the power spectral density (PSD) is normalized with the largest present peak (in this case the FB). In this way it can be seen that for the swallow tail, the shedding occurs at higher frequency and with a reduced amplitude of about 50%.

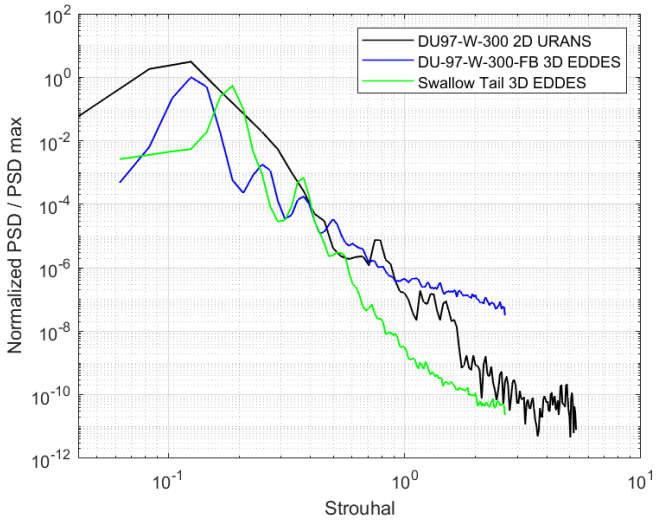

Figure 5.19: Frequency spectrum based on the C_l time series for the regular, flatback and swallow tail airfoils, $Re = 1.6 \times 10^6$, $\alpha = 11.6°$

Flow solution

In Figure 5.20d, the pressure coefficient and velocity contours obtained with the two fidelity approaches are compared. From the C_p contours, it can be seen that the EDDES predicted a lower pressure behind the TE which translates, in the velocity contours, in the vortex shedding. On the contrary, the URANS predicted a completely stable wake, very similar to the regular airfoil one and hence neglecting entirely the presence of the vortices in the wake. This shows that the 2D URANS approach is not able to capture the physics of the flow around the swallow tail.

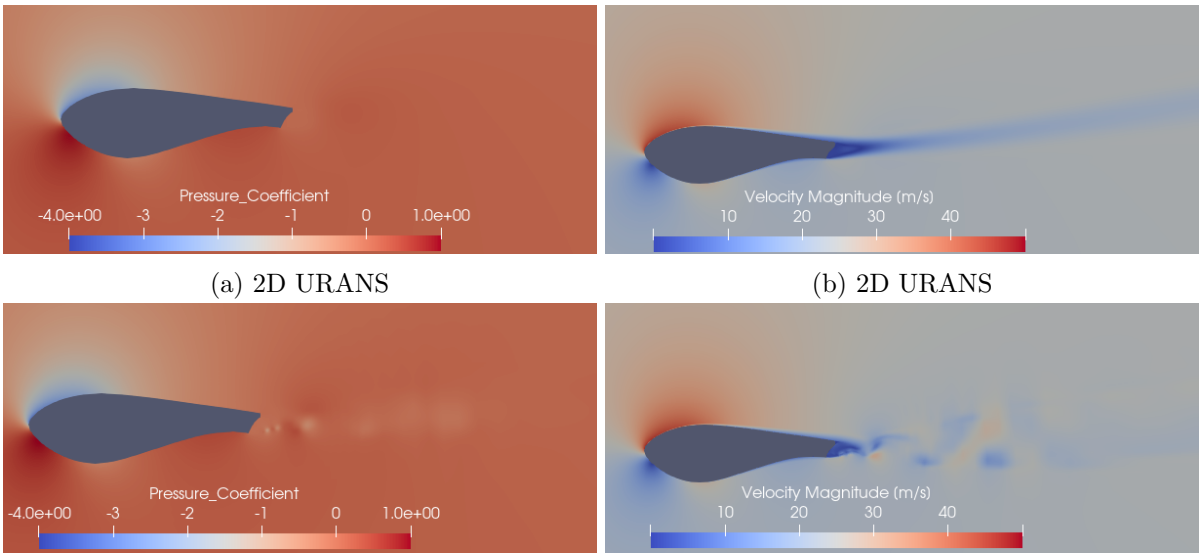

(a) 2D URANS

(b) 2D URANS

(c) 3D EDDES

(d) 3D EDDES

Figure 5.20: C_p and Velocity Contours swallow tail with different fidelity levels, $Re = 1.6 \times 10^6$, $\alpha = 11.6°$

Finally, as reflected in the Strouhal analysis, even if the swallow tail presents vortex shedding as the flatback airfoil, its extent is much more contained. This can be seen by comparing Figure 5.13d and 5.20c and Figure 5.14d and 5.20d: the pressure behind the TE of the flatback is much lower as well as the wake is much more unsteady and with larger eddies.

5.5.4 Conclusions

From the above analysis it can be concluded that EDDES is the most suitable approach for the prediction of the flow around the swallow tail. For the flatback airfoil, it has been observed that the 2D URANS were at least capable of capturing the flow phenomena involved. For the swallow tail, the 2D URANS are completely neglecting the vortex shedding in the wake, predicting instead a totally stable wake. On the other hand, the aerodynamic coefficients predicted with the 2D URANS simulations were able to give a good indications of the achievable performance of this geometry.

5.6 Polars 2D URANS: full comparison

5.6.1 Test case description

In order to showcase the advantages of the swallow tail concept, a comparison between all the airfoils involved in this study must be made for a range of angles of attack. Most of the experimental data are available at $Re = 3 \times 10^6$. The performance of the airfoils will be analyzed looking at the desirable airfoil characteristics shown in 2.1.2.
Given the large amount of simulations, these will be performed using 2D URANS. This approach,in combination with the SST turbulence model has proven to provide a good indication of the airfoil aerodynamic characteristics and hence suitable for a comparison analysis. The accuracy of URANS resulted to drop with larger level of unsteadiness. This is mainly the case for the flatback airfoil, for which experimental data are available and, hence, possible to judge the reliability of the URANS results.
The computational grids as well as the boundary conditions will be the same as the ones used in the previous 2D URANS simulations.

5.6.2 Results

The numerical results are first compared to the experimental data in order to assess their reliability. The comparison, in terms of aerodynamic coefficients, is given in Table 5.8.

Data	α [deg]	C_l	C_d	α [deg]	C_l	C_d	α [deg]	C_l	C_d
2D URANS	4	0.82	0.0596	11.05	1.69	0.0562	13.4	1.94	0.0548
experiments tripped	4.12	**0.83**	**0.0598**	11.05	**1.74**	**0.0545**	13.4	**2.03**	**0.0466**

Table 5.8: 2D URANS vs experiments DU97-W-300-FB, $Re = 3 \times 10^6$

As expected, at low AoA there is a good match between the numerical and experimental data, while the difference increases with increasing AoA. Note that for $Re = 1.6 \times 10^6$, there was no experimental tripped C_d value available. Here, for $Re = 3 \times 10^6$, it can be seen that the C_d predicted by URANS and the experimental value are within 0.003% of each other at $\alpha = 4°$ and within 0.03% at $\alpha = 11°$. The accuracy drops only at $\alpha = 13.4°$ and mainly in the drag prediction: the C_l and C_d are within 0.04% and 0.18% the experimental bounds respectively. This, shows that the 2D URANS are suitable for a comparison analysis and deriving the aerodynamic polars.

The lift and drag polars are given in Figure 5.21a and 5.21b respectively. The lift curve is steeper for the flatback airfoil, followed by the regular airfoil. The slope of the swallow tail lift curve is very close to the regular airfoil one but with higher $C_{l,max}$. With regard to the C_d, the flatback shows the largest values, which remain quite constant for a broad AoA range. On the contrary, the regular airfoil presents the lowest drag values but only up to approximately $\alpha = 9°$. The C_d values of the swallow tail are slightly higher than the regular airfoil ones and substantially lower than the flatback. Furthermore, as for the flatback, these values remain constant for a wider range of AoA. In particular, the swallow tail reduces the FB drag penalty up to 52%.

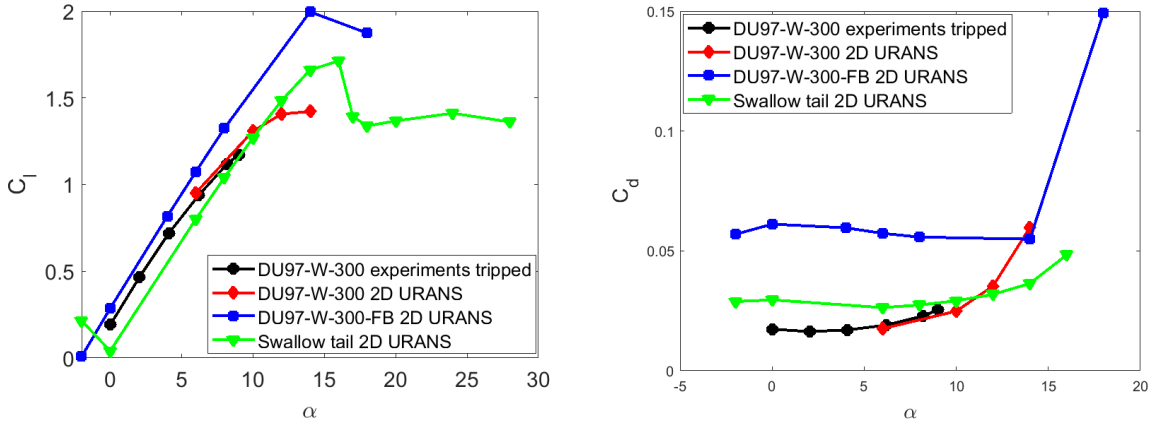

(a) $C_l - \alpha$ (b) $C_d - \alpha$

Figure 5.21: C_l vs α and C_d vs α for the regular, flatback and swallow tail airfoils, $Re = 3 \times 10^6$

The aerodynamic efficiency is shown in Figure 5.22, where it can be seen that the swallow tail concept outperforms the flatback airfoil for all the AoA, with an increase in efficiency up to 60%. At low AoA, when the flow is mainly attached, the regular airfoil shows higher efficiency while, at higher AoA, towards stall conditions, the swallow tail resulted to be the most efficient airfoil.

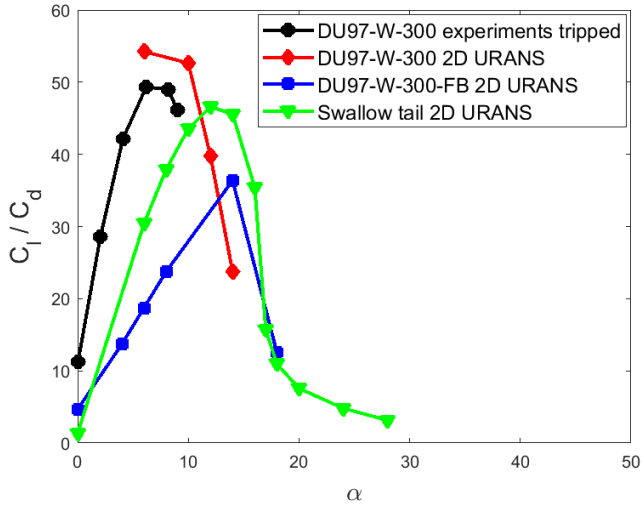

Figure 5.22: C_l/C_d for the regular, flatback and swallow tail airfoils, $Re = 3 \times 10^6$

5.6.3 Conclusions

The above analysis confirms the preliminary results given in 5.4.4 and answers the first research question. When compared to the regular airfoil, the swallow tail retains the advantages of the FB ((C.2), (C.4), (C.7)) while overcoming its drawbacks: the drag is reduced up to 52%, resulting in an increase in aerodynamic efficiency up to 60% (C.1). Overall, the regular airfoil achieved the highest C_l/C_d in attached flow conditions while, towards stall, the swallow tail gave the best performance.
The fact that the flatback airfoil presents the highest $C_{l,max}$, shows that there is still room of improvement for the swallow tail design. Indeed, as shown in 5.4.3, it is possible to increase the $C_{l,max}$ with a longer pressure side curve, thus improving further the efficiency. Already with the proposed configuration (ST2), the swallow tail shows an increase of 46% in $C_{l,max}$ compared to the regular airfoil, meaning that in the actual implementation of the ST on a wind turbine blade, a smaller chord would be needed and, hence, the blade will experience smaller standstill loads (C.4). A parameterization of the geometry involving also other design parameters, might also help in reducing the drag and hence improving the overall efficiency of the swallow tail concept. Finally, higher fidelity level simulations and/or experiments are needed to verify other important airfoil characteristics such as stall behaviour (C.5) and induced vibrations due to vortex shedding(C.6).

6 Conclusions

In the present work the flow around flatback and swallow tail airfoils for wind turbine applications has been investigated numerically. In order to do so, a suitable and efficient computational set-up able to capture the aerodynamic characteristics of these airfoils has first been researched. The fidelity levels that have been evaluated in this investigation are 2D URANS, 3D URANS and 3D EDDES as hybrid RANS/LES. With respect to the computational domain, a grid refinement study has been carried out comparing three grids with different resolution while for the 3D cases two spanwise lengths of the computational domain have been investigated investigated.
To determine the most suitable set-up, the numerical results have been judged in terms of prediction accuracy of C_l, C_d, C_p distributions, time histories, St and flow phenomena captured. On the other hand, considerations regarding the computational time have allowed to evaluate the set-up efficiency.

The flow around the flatback airfoil, compared to the regular one, is characterized by a delayed separation resulting in an larger $C_{l,max}$. However, the presence of the vortex shedding, due to the low pressure behind the trailing edge, results in a drag penalty. The 2D URANS approach in combination with the SST turbulence model has found to be an efficient method for the prediction of the aerodynamic coefficients and the main flow phenomena. However, when compared to the 3D simulations, the 3D EDDES at higher angle of attack presented a more accurate prediction of the pressure drop and the vortex shedding, thus giving the most reliable results. The two spanwise sizes tested (SW5 and SW2), were both able to capture these phenomena. With respect to the 3D URANS simulations, these have resulted to be dissipative and unable to predict the flow around FB.

To overcome the drawbacks of the flatback, two swallow tail concepts (ST1 and ST2) have been designed and their performance investigated with 2D URANS. The results have shown that the delayed separation is retained while the wake unsteadiness and drag reduced. In particular, the C_d has reduced up to 51%. Furthermore, the ST2 geometry, given the longer pressure side, provided a larger C_l than the ST1 and hence efficiency. In particular, the swallow tail, at $Re = 1.6 \times 10^6$ and for $\alpha = 11.9°$, has shown to outperform both the FB, with an efficiency increase of 43%, and the regular airfoil, with an efficiency increases of 26%. Further investigation of this geometry with 3D EDDES has shown that, even if less severe compared to the FB, the swallow tail concept also presents vortex shedding. This phenomena was completely neglected by the 2D URANS, where the predicted wake was completely stable and very similar to the regular airfoil one. Overall, compared to the 2D URANS simulations, the EDDES ones predicted larger C_d but also a larger C_l, meaning that the swallow tail concept still presented the highest efficiency. Additionally, when comparing the FB and ST results computed with 3D EDDES, the Strouhal number analysis shows that the swallow tail reduces the amplitude of the vortex of about 50% while increasing its frequency.

Finally, a comparison between all the involved geometries has been performed using 2D URANS. While it is true that 3D EDDES resulted to be the most suitable approach for capturing the flow phenomena involved, especially for the swallow tail, 2D URANS has shown to provide

aerodynamic coefficient predictions that are accurate enough to perform a comparison analysis at both $Re = 1.6 \times 10^6$ and $Re = 3 \times 10^6$. The lift and the drag coefficients for a range of angles of attack have been derived and allowed to answer the research question: the swallow tail is able to retain the advantages of the FB while overcoming its drawbacks. Indeed the drag is reduced up to 52%, resulting in an increase in aerodynamic efficiency up to 60%. Looking at the regular airfoil, it achieved the highest C_l/C_d in attached flow conditions while, towards stall, the swallow tail gave the best performance. Indeed, the proposed swallow tail shows an increase of 46% in $C_{l,max}$. The fact that the flatback airfoil presents the highest $C_{l,max}$, shows that there is still room of improvement for the swallow tail design. Hence, when assessing the properties of swallow tail in relation to the performance of wind turbine blades, it can be concluded that the swallow tail presents the following advantages:

- High efficiency (C.1)
- Reduced surface curvature towards TE (C.2)
- Increased $C_{l,max}$ (C.4)
- Enhanced structural integrity (C.7)

With respect to other important airfoil characteristics such as stall behaviour (C.5) and induced vibrations due to vortex shedding(C.6), higher fidelity level simulations and/or experiments are needed.

7 Recommendations

In this study a computational grid and two fidelity level approaches have been used to predict the flow characteristics of flatback and swallow tail airfoils. It has been shown that the swallow tail outperforms the flatback and, towards stall, also the regular airfoil. However, to further showcase the potential performance of the swallow tail and extend its applicability to also the outer part of the wind turbine blade, the following additional investigations and suggestions are made:

- Perform an experimental campaign of the swallow tail design. This would allow to better assess the potential of this concept, including important aspects such as stall behaviour and vibrations, and to validate the numerical results.
- Perform EDDES simulations of the FB and swallow tail for a range of AoA and at larger Re. For $\alpha = 11.6°$ and $Re = 1.6 \times 10^6$, the 2D URANS and 3D EDDES predictions of the aerodynamic coefficients were not differing significantly. This does not mean it is the case at higher Re and for other angles of attack for which different conclusions might be derived. Furthermore, performing higher fidelity level simulations of the ST for a larger range of angles of attack and Reynolds number allows to better assess the potential of this concept. Once the characteristics of the flow around the swallow tail are better outlined together with a parameterization of the geometry, it will be possible to check whether this concept can be extended to the outer part of the blade.
- Design a swallow tail for another airfoil. It has been shown that the swallow tail outperforms the performance of the DU97-W-300-FB. However, for a proof of concept, a swallow tail design should be made for at least one other airfoil.
- A time refinement study and spanwise grid refinement study should have been carried out also for the EDDES cases. This will allow to assess the reliability of the obtained results. Eventually, a better correspondence between the experimental and numerical St can also be achieved. Several time steps and a finer spanwise grid size have been tested but no converged results have been achieved.
- Perform the time refinement with non dimensional time steps. A time refinement study for the DU-97-W-300-FB has been performed at $Re = 1.6 \times 10^6$ from which an optimal time step has been found and used also for the simulations at $Re = 3 \times 10^6$. Instead, the analysis should have been carried out by defining a non-dimensional time step $\tilde{dt} = \frac{dt}{t_c}$, where dt is the actual time step size (sec) and t_c is the convective time scale (sec), with $t_c = \frac{c}{U_\infty}$. For $Re = 1.6 \times 10^6$ the free stream velocity is $U_\infty = 23.54 m/s$, while for $Re = 3 \times 10^6$ is $U_\infty = 44.13 m/s$. Hence, the optimal dimensional time step $dt = 0.0003$ corresponds to a non dimensional time step $\tilde{dt} = 0.007$, which, translated back in dimensional form for the higher Re, corresponds to $dt = 0.00016$.

References

[1] J. F. Manwell, J. G. McGowan, and A. L. Rogers, *Wind Energy Explained: Theory, Design and Application*. 2010.

[2] D. A. Johnson, M. Gu, and B. Gaunt, "Wind turbine performance in controlled conditions: BEM modeling and comparison with experimental results," *International Journal of Rotating Machinery*, vol. 2016, 2016.

[3] K. J. Standish and C. P. V. Dam, "Aerodynamic analysis of blunt trailing edge airfoils," *Journal of Solar Energy Engineering, Transactions of the ASME*, vol. 125, pp. 479–487, 2003.

[4] J. H. Ferziger, M. Perić, and R. L. Street, *Computational Methods for Fluid Dynamics*. Springer Cham, 4 ed., 2009.

[5] W. A. Timmer and R. P. V. Rooij, "Summary of the Delft University wind turbine dedicated airfoils," *Journal of Solar Energy Engineering, Transactions of the ASME*, vol. 125, pp. 488–496, 11 2003.

[6] J. P. Baker, E. A. Mayda, and C. P. V. Dam, "Experimental and computational analysis of thick flatback wind turbine airfoils," 2006.

[7] M. F. Barone, D. E. Berg, W. J. Devenport, and R. Burdisso, "Aerodynamic and aeroacoustic tests of a flatback version of the DU97-W-300 airfoil," *Technical Report No. SAND2009-4185, Sandia National Laboratory*, 2009.

[8] J. P. Baker, van Dam, and B. L. Gilbert, "Flatback airfoil wind tunnel experiment," 2008.

[9] M. Manolesos and S. G. Voutsinas, "Experimental study of drag-reduction devices on a flatback airfoil," vol. 54, pp. 3382–3396, American Institute of Aeronautics and Astronautics Inc., 2016.

[10] F. Grasso, "Swallow tail airfoil," vol. United States Patent US0238298A1, 2018.

[11] O. C. Yilmaz and W. A. Timmer, "Experimental evaluation of a non-conventional flat back thick airfoil concept for large offshore wind turbines," American Institute of Aeronautics and Astronautics Inc, AIAA, 2018.

[12] C. Stone, M. Barone, C. E. Lynch, and M. J. Smith, "A computational study of the aerodynamics and aeroacoustics of a flatback airfoil using hybrid rans-les," 2009.

[13] G. Papadakis, M. Manolesos, K. Diakakis, and V. A. Riziotis, "DES vs RANS: The flatback airfoil case," vol. 1618, IOP Publishing Ltd, 9 2020.

[14] M. Manolesos and G. Papadakis, "Investigation of the three-dimensional flow past a flatback wind turbine airfoil at high angles of attack," *Physics of Fluids*, vol. 33, 8 2021.

[15] B. Stoevesandt, G. Schepers, P. Fuglsang, and Y. Sun, "Handbook of wind energy aerodynamics," 2022.

[16] C. Bak, *Aerodynamic design of wind turbine rotors*, pp. 59–108. Elsevier Inc., 2013.

[17] S. F. HOERNER, "Base drag and thick trailing edges," *Journal of the Aeronautical Sciences*, vol. 17, pp. 622–628, 10 1950.

[18] F. Grasso and O. Ceyhan, "Non-conventional flat back thick airfoils for very large offshore wind turbines," American Institute of Aeronautics and Astronautics Inc., 2015.

[19] S. P. Law and G. M. Gregorek, "Wind tunnel evaluation of a truncated NACA 64-621 airfoil for wind turbine applications," 1987.

[20] M. F. Barone and D. Berg, "Aerodynamic and aeroacoustic properties of a flatback airfoil: An update," 2008.

[21] F. Palacios, T. D. Economon, A. Aranake, S. R. Copeland, A. K. Lonkar, T. W. Lukaczyk, D. E. Manosalvas, K. R. Naik, S. Padron, B. Tracey, A. Variyar, and J. J. Alonso, "Stanford university unstructured (SU2): Analysis and design technology for turbulent flows," American Institute of Aeronautics and Astronautics, 1 2014.

[22] P. Spalart and S. Allmaras, "A one-equation turbulence model for aerodynamic flows," *30th Aerospace Sciences Meeting and Exhibit*, 1992.

[23] F. R. Menter, "Two-equation eddy-viscosity turbulence models for engineering applications," *AIAA Journal*, vol. 32, pp. 1598–1605, 1994.

[24] O. Guerri, K. Bouhadef, and A. Harhad, "Turbulent flow simulation of the NREL S809 airfoil," *Wind Engineering*, vol. 30, 05 2006.

[25] P. Spalart, W.-H. Jou, M. Strelets, and S. Allmaras, "Comments on the feasibility of LES for wings, and on a hybrid RANS/LES approach," 01 1997.

[26] P. R. Spalart, S. Deck, M. L. Shur, K. D. Squires, M. K. Strelets, and A. Travin, "A new version of detached-eddy simulation, resistant to ambiguous grid densities," *Theoretical and Computational Fluid Dynamics*, vol. 20, pp. 181–195, 7 2006.

[27] "Hybrid RANS/LES calculations in SU2," American Institute of Aeronautics and Astronautics Inc, AIAA, 2017.

[28] M. L. Shur, P. R. Spalart, M. K. Strelets, and A. K. Travin, "An enhanced version of DES with rapid transition from RANS to LES in separated flows," *Flow, Turbulence and Combustion*, vol. 95, pp. 709–737, 12 2015.

[29] P. P. Nataraj, "Airfoil self-noise predictions using ddes and the fwh analogy," *Msc Thesis, University of Twente*, 2022.

[30] T. M. Inc., "Matlab version: 9.13.0 (r2022b)," 2022.

[31] T. Winnemöller and C. P. V. Dam, "Design and numerical optimization of thick airfoils including blunt trailing edges," *Journal of Aircraft*, vol. 44, 2007.

[32] T. D. Economon, F. Palacios, S. R. Copeland, T. W. Lukaczyk, and J. J. Alonso, "SU2: An open-source suite for multiphysics simulation and design," *AIAA Journal*, vol. 54, pp. 828–846, 2016.

[33] F. Palacios, M. R. Colonno, A. C. Aranake, A. Campos, S. R. Copeland, T. D. Economon, A. K. Lonkar, T. W. Lukaczyk, T. W. Taylor, and J. J. Alonso, "Stanford university unstructured (SU2): An open-source integrated computational environment for multi-physics simulation and design," 2013.

[34] A. Jameson and Sriram, "An assessment of dual-time stepping, time spectral and artificial compressibility based numerical algorithms for unsteady flow with applications to flapping wings," *19th AIAA Computational Fluid Dynamics Conference*, 2009.

[35] Cadence, "Pointwise version: 2022.2," 2022.

[36] R. Van Rooij, "Modification of the boundary layer calculation in RFOIL for improved airfoil stall prediction," Sep 1996.

[37] M. Drela, "XFOIL 6.94 user guide," *Aeronautics and Astronautics Dept., Massachusetts Inst. of Technology, Cambridge, MA*, 2001.

[38] F. Grasso, "Modeling and effects of base drag on thick airfoils design," American Institute of Aeronautics and Astronautics Inc., 2014.